Progress in Oceanography 204 (2022) 102808

Contents lists available at ScienceDirect

Progress in Oceanography

journal homepage: www.elsevier.com/locate/pocean

Synchronized decadal variabilities in the Kuroshio and Kuroshio Extension system

Yu-Xiang Qiao [a], Hirohiko Nakamura [a,b,*], Shinichiro Kako [c], Ayako Nishina [b], Tomohiko Tomita [d]

[a] The United Graduate School of Agricultural Sciences, Kagoshima University, Kagoshima, Japan
[b] Faculty of Fisheries, Kagoshima University, Kagoshima, Japan
[c] Graduate School of Science and Engineering, Kagoshima University, Kagoshima, Japan
[d] Faculty of Advanced Science and Technology, Kumamoto University, Kumamoto, Japan

ARTICLE INFO

Keywords:
Air-sea interaction
Decadal variability
Mesoscale eddies
North Pacific
Rossby waves
Satellite altimetry
Western boundary currents

ABSTRACT

Using satellite altimetry and wind stress data, the spatially coherent decadal variabilities in current intensity and current path during 1993–2018 were investigated for a western boundary current system, namely, the Kuroshio from the east of Luzon Island to the south of Japan and the Kuroshio Extension (KE). Analyses based on Hovmöller diagrams showing decadal variabilities along the entire current demonstrated three types of synchronic relationship between different regions: 1) an out-of-phase relationship in current intensity between the Kuroshio south of Japan and the KE during 1993–2018; 2) an out-of-phase relationship in current intensity between the Kuroshio from the east of Taiwan (ETW) to the East China Sea (ECS) and the KE during 2006–2014; 3) an out-of-phase relationship in current position between the Kuroshio paths in the ETW to ECS and the Luzon Strait during 1993–2018. These patterns were dynamically regulated by the Pacific Decadal Oscillation (PDO). The synchronized current-intensity variability in 2006–2014, which governed almost the entire current system, was caused by coherent phenomena comprising two kinds of baroclinic Rossby wave propagations along the KE and the subtropical countercurrent (STCC), and a regional sea surface height (SSH) anomaly advection from the South China Sea (SCS) to the ECS via the Taiwan Strait. However, the synchronized current-path variability between 1993 and 2018 was caused by an SSH anomaly migration advected by the Kuroshio from the western North Equatorial Current zone to the ECS and an SSH variability localized in the SCS.

In this study, we paid particular attention to that the current intensity of the Kuroshio in the ETW to ECS had a positive no-lag correlation with the SSH-based PDO index in 1996–2005 while a positive 3–4 years lag correlation with that index during 2006–2014. It was emphasized that this transition was due to the following mechanism: the current-intensity variability in 1996–2005 was mainly caused by the variability of the eddy activity in the western STCC zone, while that variability in 2006–2014 was mainly caused by the amplification of baroclinic Rossby waves propagating along the STCC zone; the shift from the former to the latter was generated by a rapid phase shift with a relatively large amplitude for the wind stress curl anomaly and a timescale change of the eddy kinetic energy over the STCC zone around 2006.

1. Introduction

The Kuroshio and Kuroshio Extension (KE) serve as the western boundary current of the North Pacific subtropical gyre. The entire path of this Kuroshio and KE System (hereafter, Kuroshio–KE System) is shown in Fig. 1 along with the names of the geographical areas comprising the system: namely, the east of Luzon Island (ELI), Luzon Strait (LS), east of Taiwan (ETW), East China Sea (ECS), south of Japan

Abbreviations: CEOF, Complex Empirical Orthogonal Function; CMEMS, Copernicus Marine and Environment Monitoring Service; ECS, East China Sea; EKE, Eddy kinetic energy; ELI, East of Luzon Island; EOF, Empirical Orthogonal Function; ETW, East of Taiwan; IFREMER, National Institute for Ocean Science; KE, Kuroshio Extension; LS, Luzon Strait; NEC, North Equatorial Current; PC, Principal component; PDO, Pacific Decadal Oscillation; SCS, South China Sea; SJ, South of Japan; SSH, Sea surface height; SSHA, Sea surface height anomaly; STCC, Subtropical countercurrent.

* Corresponding author at: Faculty of Fisheries, Kagoshima University, Kagoshima, Japan.
E-mail address: nakamura@fish.kagoshima-u.ac.jp (H. Nakamura).

https://doi.org/10.1016/j.pocean.2022.102808
Received 14 July 2021; Received in revised form 18 April 2022; Accepted 25 April 2022
Available online 28 April 2022

(SJ), and KE. Because the Kuroshio–KE System is mainly driven by the Westerlies and the Trades over the North Pacific Ocean, changes in these prevailing winds can cause variabilities in the current intensity and current position of the Kuroshio–KE System on several timescales. Furthermore, it has been suggested that the changes in this current system affect the atmospheric circulation patterns around the North Pacific Ocean on decadal timescales through oceanic heat redistribution (e.g., Qiu et al., 2014). Understanding the mechanisms that drive decadal variability of the Kuroshio–KE System is essential for understanding the North Pacific modes of climate variability such as the Pacific Decadal Oscillation (PDO) (Mantua and Hare, 2002). Following these scenarios, many previous studies have investigated regional features of the Kuroshio (e.g., see Nakamura (2020) for a review) and the KE (e.g., Qiu et al., 2020). However, there is still a lack of knowledge about synchronized decadal variabilities between different regions in the Kuroshio–KE System. Hence, in the present study, we will investigate the synchronized features of decadal variabilities in current intensity and current position over the Kuroshio–KE System.

Previous studies on the decadal variability of the KE have shown that the KE strengthened (weakened) along with northward (southward) current-path shifts, lagging the PDO-related wind stress curl anomalies over the eastern North Pacific by 3–4 years (Deser et al., 1999; Qiu, 2003; Qiu and Chen, 2005; Taguchi et al., 2007; Sasaki and Schneider, 2011; Sasaki et al., 2013). Baroclinic Rossby waves played an important role in forming this oceanic variability because they carried the sea surface height (SSH) anomalies induced by wind stress curl changes; the westward-propagating positive (negative) SSH anomalies strengthened (weakened) the southern recirculation of the KE, and thus resulted in the strengthening (weakening) of the KE (e.g., Qiu and Chen, 2005). Furthermore, the baroclinic Rossby waves shifted the Kuroshio in the SJ (hereafter, SJ-Kuroshio) toward a deep nearshore (shallow offshore) channel over the Izu–Ogasawara Ridge, causing the KE path to be stable (unstable) (Qiu and Chen, 2005; Sugimoto and Hanawa, 2011; Usui et al., 2013). However, a recent study (Qiu et al., 2020) found that, instead of the baroclinic Rossby waves, the stable large meander of the SJ-Kuroshio, which appeared in August 2017, has played a crucial role in strengthening the KE since August 2017, which was due to the stable large meander path having fixed the position of the Kuroshio at a deep nearshore channel over the Izu–Ogasawara Ridge.

Besides the KE, many researchers have investigated the interannual to decadal volume transport variability of the Kuroshio in connection with the PDO index. Using satellite altimetry and tide gauge data, Han and Huang (2008) showed that the PDO affected the SSH on the continental shelf in the ECS with a negative correlation between 1993 and 2002, resulting in a Kuroshio transport variability in the ECS with a positive correlation. In addition, using data from 1993 to 2008, Andres et al. (2011) ascribed such a positive correlation to Kuroshio's barotropic response to the PDO-related wind stress curl in the interior North Pacific. However, studies (e.g., Nakamura et al., 2012) pointed out that the Kuroshio transport in the ECS is no longer correlated at zero lag with the PDO index since the 2000s, and it was suggested that this disconnection was caused by the effect of enhanced mesoscale eddy activity in the subtropical countercurrent (STCC) zone (Soeyanto et al., 2014). On the other hand, Yan et al. (2016) suggested that the eddy kinetic energy (hereafter, EKE) in the STCC always affected the Kuroshio inflow volume from the ETW to ECS with a positive correlation using data from 1993 to 2011. In addition, it has been shown that the EKE in the STCC zone was positively correlated with the PDO index during 1993–2011 (Qiu and Chen, 2013), implying that the eddy activity should not be regarded as a reason for the disappeared correlation between the Kuroshio transport and the PDO index since the 2000s. Therefore, the mechanism for the interannual to decadal Kuroshio variability over the area from the ETW to ECS is still uncertain.

Regarding variabilities on decadal timescale, it has not yet been established whether the Kuroshio–KE System responds with uniform spatial and temporal patterns throughout or whether different subsystems respond differently. Therefore, in Sections 2.1 and 2.2, the Kuroshio and KE decadal variabilities are synthesized by Hovmöller diagrams along an entire length of this current system. Moreover, in Section 2.3, we define a new climate index dynamically consistent with the geostrophic velocity based on SSH data. In Section 2.4, we derive a simple baroclinic Rossby wave propagation model used as an analytical tool in this study. In Section 3, we exhibit the synchronized decadal variabilities in the Kuroshio–KE System, especially focusing on the phenomenon that the transport of the Kuroshio in the ECS lost the positive no-lag correlation with the PDO index since the 2000s, and

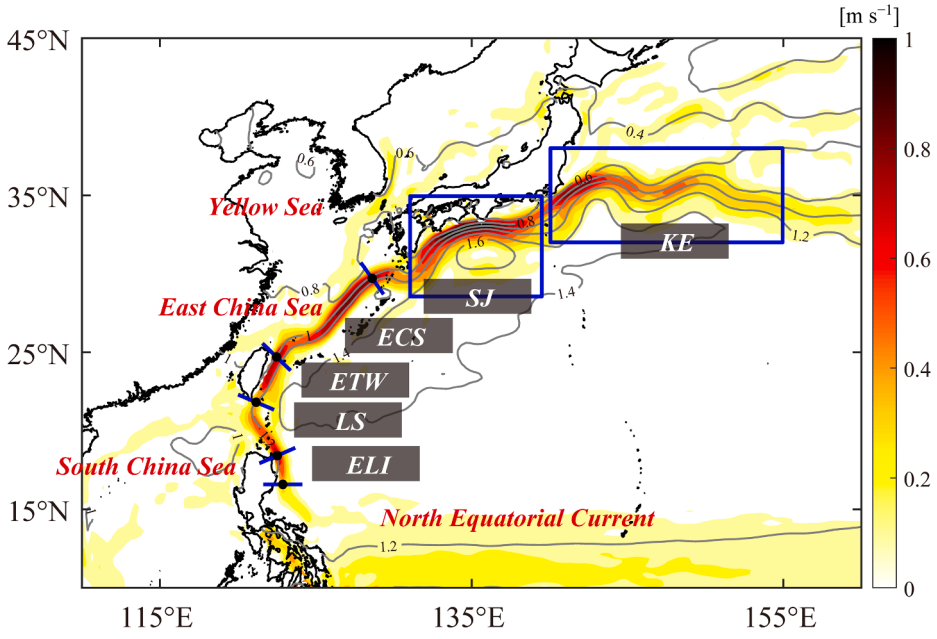

Fig. 1. Distributions for the SSH (m; gray contour) and the absolute surface geostrophic velocity (m s^{-1}; color) around the Kuroshio–KE System averaged in 1993–2018. The regional names of the Kuroshio–KE System are denoted by the following abbreviations. ELI: east of Luzon Island; LS: Luzon Strait; ETW: east of Taiwan; ECS: East China Sea; SJ: south of Japan; KE: Kuroshio Extension.

elaborate the relevant mechanisms in which two types of PDO-related baroclinic Rossby waves passing through the STCC zone and KE zone caused the synchronization between the Kuroshio and KE current intensities. Section 4 discusses the synchronized current-position variability in the Kuroshio–KE system and the influence of wind change over the North Pacific upon the Kuroshio–KE system. The findings from this study are finally concluded in Section 5.

2. Data and methods

2.1. Observational datasets and preliminary data processing

To investigate decadal variability of the Kuroshio–KE System, we used satellite altimetry SSH data processed by Ssalto/Duacs and distributed by the Copernicus Marine and Environment Monitoring Service (CMEMS, https://marine.copernicus.eu/). Surface geostrophic velocity data derived from SSH, which are approximately proportional to the volume transport in the upper layer, were used to estimate the strength and position of the Kuroshio–KE System. This satellite altimetry dataset has a daily temporal resolution from January 1993 to December 2018 and a 1/4-degree horizontal resolution.

To examine dynamical relationships of decadal variability of the Kuroshio–KE System with the wind forcing in the North Pacific, we used the wind stress vector data from WIND GLO WIND L4 REP OBSERVATIONS 012 006 datasets that were produced by National Institute for Ocean Science (IFREMER, https://wwz.ifremer.fr/en/) and distributed by CMEMS. This wind dataset production has a 6-hour temporal resolution from January 1992 to December 2018 and a 1/4-degree horizontal resolution.

Our interest is in decadal-scale variability in the Kuroshio–KE System. Therefore, temporal variabilities with >4 years were first extracted from annually-averaged surface geostrophic velocity and SSH data by applying a 4-year second-order forward-backward Butterworth filter. Such a 4-year low-pass filter was suitable for eliminating the interannual variability with a 2–3 years period from the original data. This paper's results were derived from the 4-year low-pass filtered satellite altimetry data except for an EKE estimation in Section 3.4. In addition, a globally averaged SSH anomaly, which is regarded as a global sea-level rise component, was excluded from the filtered SSH anomaly for each year. Hereafter, the SSH anomaly with this treatment is expressed as SSHA in this paper.

2.2. Hovmöller diagram along the Kuroshio–KE System

Hovmöller diagrams were used to display temporal and spatial variabilities of the current speed and current position upon a stream coordinate along the Kuroshio–KE System. The Kuroshio in the upstream area (ELI to ECS) was relatively stable along the continental slope except for the LS. In contrast, the SJ-Kuroshio and the KE in the downstream area were unstable due to larger meandering motions. Therefore, to create the Hovmöller diagrams, different methods were applied to the upstream and downstream areas.

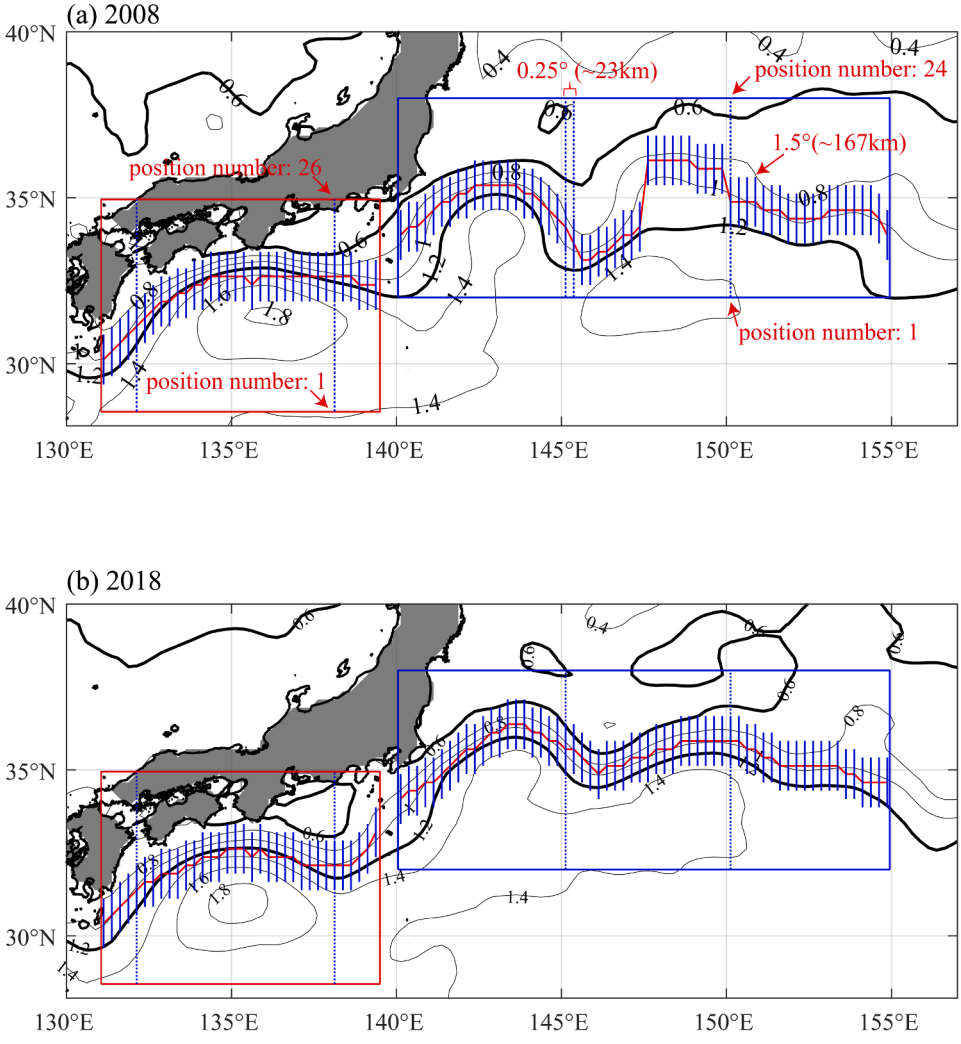

Fig. 2. SSH distributions (m; black contours) around the KE (blue rectangle) and SJ-Kuroshio (red rectangle) in 2008 (a) and 2018 (b), and the thick contours denote the 0.6 m and 1.2 m SSH; the dashed blue lines denote the meridional sections that are utilized to extract the current speed and position for the KE and SJ-Kuroshio between 1993 and 2018; the solid blue lines denote the locations where the velocities are used to estimate the annual mean for the speed of the KE and SJ-Kuroshio in 2008 (a) and 2018 (b); the red lines denote the current positions of the KE and SJ-Kuroshio in 2008 (a) and 2018 (b). (For interpretation of the references to color in this figure legend, the reader is referred to the web version of this article.)

Over the downstream area, the current directions of the Kuroshio and the KE were almost eastward; thus, the current speed and current position were determined on meridional sections with a zonal interval of 0.25° (~23 km) for each year during 1993–2018 (see Fig. 2a). The following procedures were carried out after the velocity field in the downstream area was running-averaged with a distance of 1.5° (~167 km) along each meridional section: Over the KE area, the large SSH standard deviation existed in the domain between the contours of 0.6 m and 1.2 m mean SSH (figure not shown); hence the current speed and current position were defined as the maximum speed and the position with such a speed between the 0.6 m and 1.2 m contours upon each meridional section, respectively. The same method was applied to the SJ-Kuroshio, except for the domain where SSH > 0.6 m was used. The position number was given along each meridional section as 1 at the southernmost position and 24 (26) at the northernmost position for KE (SJ); one grid was equal to ~ 28 km. For example, Fig. 2 shows the meridional sections (dashed blue lines) and the stream coordinates (solid blue lines) created for 2008 and 2018.

Unlike the Kuroshio and KE over the downstream area, the Kuroshio over the upstream area was relatively stable in the position with a steady northwestward or northeastward velocity direction; thus, cross-sections perpendicular to a mean streamline were firstly created according to the following steps: 1) Using velocity data averaged in 1993–2018, the position with maximum speed was determined along the Kuroshio path on each zonal section with a meridional interval of 0.25°; 2) A smoothed streamline could be obtained after these positions were processed by a 9-point second-order forward-backward Butterworth low-pass filter; 3) 74 points with a 25-km spatial interval were allocated on this streamline, and a cross-section with a length of 2.5° (~250 km) perpendicular to the streamline was created at each point. This set of cross-sections (blue lines in Fig. 3) was used to extract speed and position for the Kuroshio over the upstream. The Kuroshio position at each cross-section was determined as the maximum speed location for each year within 1993–2018. The position number was given along each cross-section as −125 (1 2 5) at the offshore side (inshore side); one grid was equal to ~ 1 km. As an example, the current position (green line) for 2018 is shown in Fig. 3. The current speed along the Kuroshio was calculated by averaging the data with a speed of > 0.25 m s^{-1} on each cross-section.

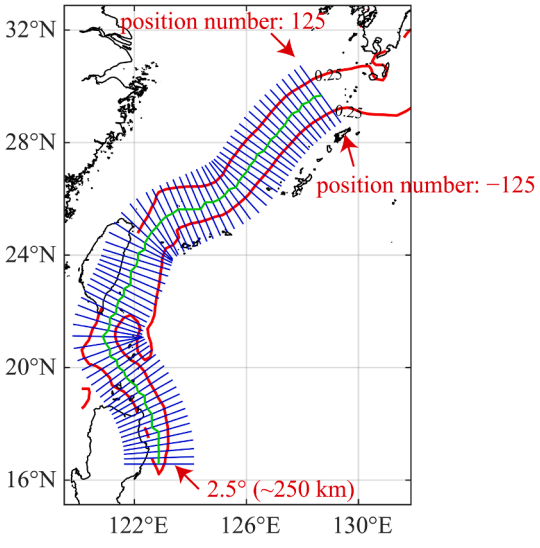

Fig. 3. Stream coordinate for the Kuroshio in the area from the ELI to ECS. The blue lines denote the cross-sections that are utilized to extract the current speed and position for the Kuroshio in ELI–ECS during 1993–2018; the green line denotes the Kuroshio position in 2018, and the red lines delimit the area with the absolute sea surface geostrophic velocity of > 0.25 m s^{-1} in 2018. (For interpretation of the references to color in this figure legend, the reader is referred to the web version of this article.)

2.3. Climate index based on SSHA

A climate index that governs decadal oceanic circulations over the North Pacific is needed to understand the generation mechanisms of the decadal variabilities in the Kuroshio–KE System. For this purpose, most previous studies have conveniently used the PDO index (Mantua and Hare, 2002), which was defined as the first mode (mode-1) of the Empirical Orthogonal Function (EOF) analysis to the sea surface temperature over the North Pacific (north of 20°N). Instead of the PDO index, a new climate index was defined in this study using SSH data because the SSH is dynamically consistent with the surface geostrophic velocity field over the Kuroshio–KE System.

We defined SSH-based PDO (PDO_{SSH}) as the mode-1 (accounts for 41.1% of the total variance) of the EOF analysis to the normalized SSHA over the entire North Pacific (0°N–60°N, 100°E–100°W). The temporal and spatial features of the PDO_{SSH} are shown in Fig. 4. The correlation coefficient of the PDO_{SSH} index with the conventional PDO index (provided by NOAA, https://www.noaa.gov/) is 0.90, which exceeded the 90% confidence level; all confidence levels for the correlation coefficients in this study were calculated based on the Monte Carlo test, in which 10,000 random time series characterized by red noise spectra similar to the original time series spectrum were used. The red noise was produced using a red noise model:

$$\begin{cases} R_1 = W_1 \\ R_{n+1} = rR_n + \sqrt{1-r^2}\,W_{n+1}, n \geq 1. \end{cases} \quad (1)$$

Here, R is a generated red noise, W is a white noise that consists of normally distributed random numbers, and r is the lag-1 autocorrelation coefficient of the original time series. The spatial distribution of mode-1 north of 20°N is well consistent with the spatial pattern of the conventional PDO. Fig. 4a denotes the main generation areas of SSHA that affected the decadal–interdecadal variabilities in the Kuroshio–KE System (the details will be explained in the following sections), namely, A: subtropical countercurrent (STCC) zone, B: western North Equatorial Current (NEC) zone, C: northeastern interior region, D: southeastern interior region.

2.4. Baroclinic Rossby wave propagation model

To examine the roles of the wind forcing in the decadal variabilities of the Kuroshio–KE System, we hindcasted the SSHA variability from the surface wind stress anomaly variability using a 1½ layer reduced-gravity model:

$$\frac{\partial \eta}{\partial t} - c_R \frac{\partial \eta}{\partial x} = -\frac{g'}{\rho_0 g f} curl\boldsymbol{\tau}, \quad (2)$$

here η is SSHA, c_R is a propagation speed of extremely long baroclinic Rossby wave, g' is the reduced-gravity, $\boldsymbol{\tau}$ is the wind stress anomaly vector, ρ_0 is the reference density, g is the gravity, f is the Coriolis parameter, x is the zonal coordinate (positive: eastward), and t is the time. The temporal and spatial SSHA variability was obtained by integrating Eq. (2) from the eastern boundary (x_e) along baroclinic Rossby wave characteristics:

$$\eta(x,y,t) = \frac{g'}{\rho_0 g f c_R}\int_{x_e}^{x} curl\boldsymbol{\tau}(x',y,t+\frac{x-x'}{c_R})dx'. \quad (3)$$

Here, SSHA variability emanated from the eastern boundary was ignored according to Qiu (2003), g' was given as 0.03 m s^{-2} (Qiu, 2002), and c_R was given based on Chelton and Schlax (1996, see their Fig. 5A). In this study, we hindcasted the SSHA variability during 1992–2018 using monthly wind stress anomaly data.

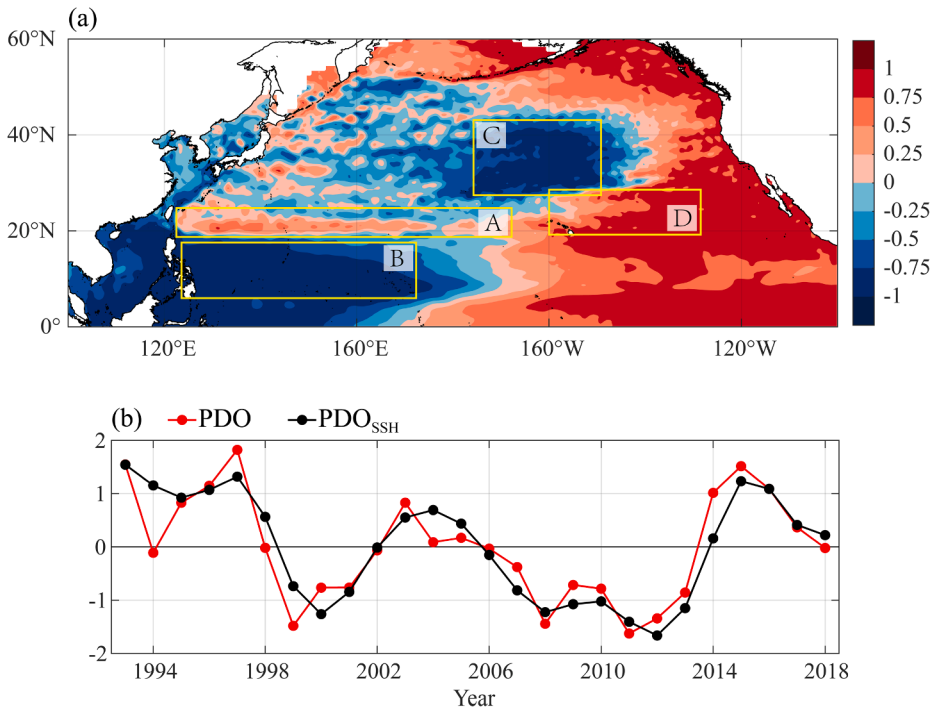

Fig. 4. EOF mode-1 for the normalized SSHA over the North Pacific (0°N–60°N, 100°E–100°W). (a) Spatial pattern of EOF-1 (41.1%); the yellow rectangles denote the regions where the SSHA focused on in this study emanated (see text for details): A: subtropical countercurrent (STCC) zone; B: western North Equatorial Current (NEC) zone; C: northeastern interior region; D: southeastern interior region. (b) The PDO_{SSH} index (black line) and conventional annual PDO index (red line). (For interpretation of the references to color in this figure legend, the reader is referred to the web version of this article.)

3. Results

3.1. Synchronized variabilities in the Kuroshio–KE System based on Hovmöller diagrams

Temporal and spatial features of decadal current speed in the Kuroshio–KE System were examined using the Hovmöller diagram (Fig. 5a). The speed variability in the KE was characterized by the following temporal and spatial features: it was strengthened in the periods of 1993–1995, 2001–2005, and 2011–2018, and weakened in the periods of 1996–2000 and 2006–2010. This temporal variability is consistent with the result shown in Qiu et al. (2020, see their Fig. 4a). Furthermore, the KE current speed was noticeably stronger upstream than downstream, while the Kuroshio became stronger from upstream to downstream. These features are consistent with the spatial distribution for the averaged velocity field denoted in Fig. 1. Because of relatively small fluctuations, the temporal variability in the speed cannot be recognized clearly over the upstream Kuroshio area from the ELI to ECS (see Fig. 5b for the standard deviation distribution). Therefore, the temporal variability of the current-speed anomaly was normalized at each position on the stream coordinate to distinguish strengthened and weakened periods clearly. Hereafter, the normalized current-speed anomaly is expressed by current intensity. As a result, Fig. 5c reveals that the Kuroshio–KE System is comprised of 3 subsystems, namely, 1) northern subsystem where intensities of the SJ and KE varied with an almost out-of-phase relationship, 2) central subsystem where intensities of the ETW and ECS varied with a clear in-phase relationship, 3) southern subsystem where intensities of the ELI and LS varied with an almost in-phase relationship.

Decadal variability of current position along the Kuroshio–KE System was also examined using the Hovmöller diagram. Fig. 5d displays the normalized current-position anomaly on each meridional section (Fig. 2) or cross-section (Fig. 3). Fig. 5e, showing the standard deviations of the position variabilities in the distance (km), indicates that the amplitude of the current-path displacement in the SJ–KE area was about ten times as large as that in the ELI–ECS area. The positive (negative) value in Fig. 5d signifies that the current shifted northward (southward) for the KE and in-shoreward (off-shoreward) for the Kuroshio. The current position could also be classified into the three subsystems mentioned above.

The EOF analysis was independently applied to the variabilities (Fig. 5c and d) of each subsystem. Fig. 6a–c shows the reconstructed leading EOF modes of the current intensities in the northern, central, and southern subsystems, respectively. Hereafter, they are called mode-1_{NI}, mode-1_{CI}, and mode-1_{SI}, respectively. These modes accounted for 53.4%, 55.6%, and 56.2% of the total variance, respectively. In addition, Fig. 6d–f shows the reconstructed leading EOF modes of the current-position anomalies in the northern, central, and southern subsystems (hereafter called mode-1_{NP}, mode-1_{CP}, and mode-1_{SP}, respectively); these leading EOF modes accounted for 44.0%, 49.2%, and 40.2% of the total variance, respectively. Besides the leading EOF modes, the contribution ratios of the mode-2s and mode-3s to the total variance are shown in Table 1. However, we focused on only the leading EOF modes in this study because they captured most of the remarkable decadal–interdecadal variabilities in the original Hovmöller diagrams (Fig. 5).

The current intensity in the northern subsystem (Fig. 6a) varied with a clear out-of-phase relationship between the KE and SJ-Kuroshio on a decadal timescale; this clear relationship has not yet been reported by previous studies. On the other hand, the current intensity in the central subsystem (Fig. 6b) varied with an in-phase relationship between the ETW and ECS, and the current intensity in the southern subsystem (Fig. 6c) also varied with an in-phase relationship between the ELI and LS. There was no coherent current-intensity relationship among the three subsystems throughout a total analysis period of 1993–2018 (Fig. 6a–c).

The synchronized features of the current-position variabilities among the three subsystems were characterized with different tendencies from the synchronized features of the current-intensity variabilities. The current-position anomaly in the northern subsystem (Fig. 6d) was incoherent with that in both the central (Fig. 6e) and southern subsystems (Fig. 6f). However, the variability in the central subsystem (Fig. 6e) had an out-of-phase relationship with that of the LS in the southern subsystem (Fig. 6f) except for the period 1998–2002 when such a relation was unclear.

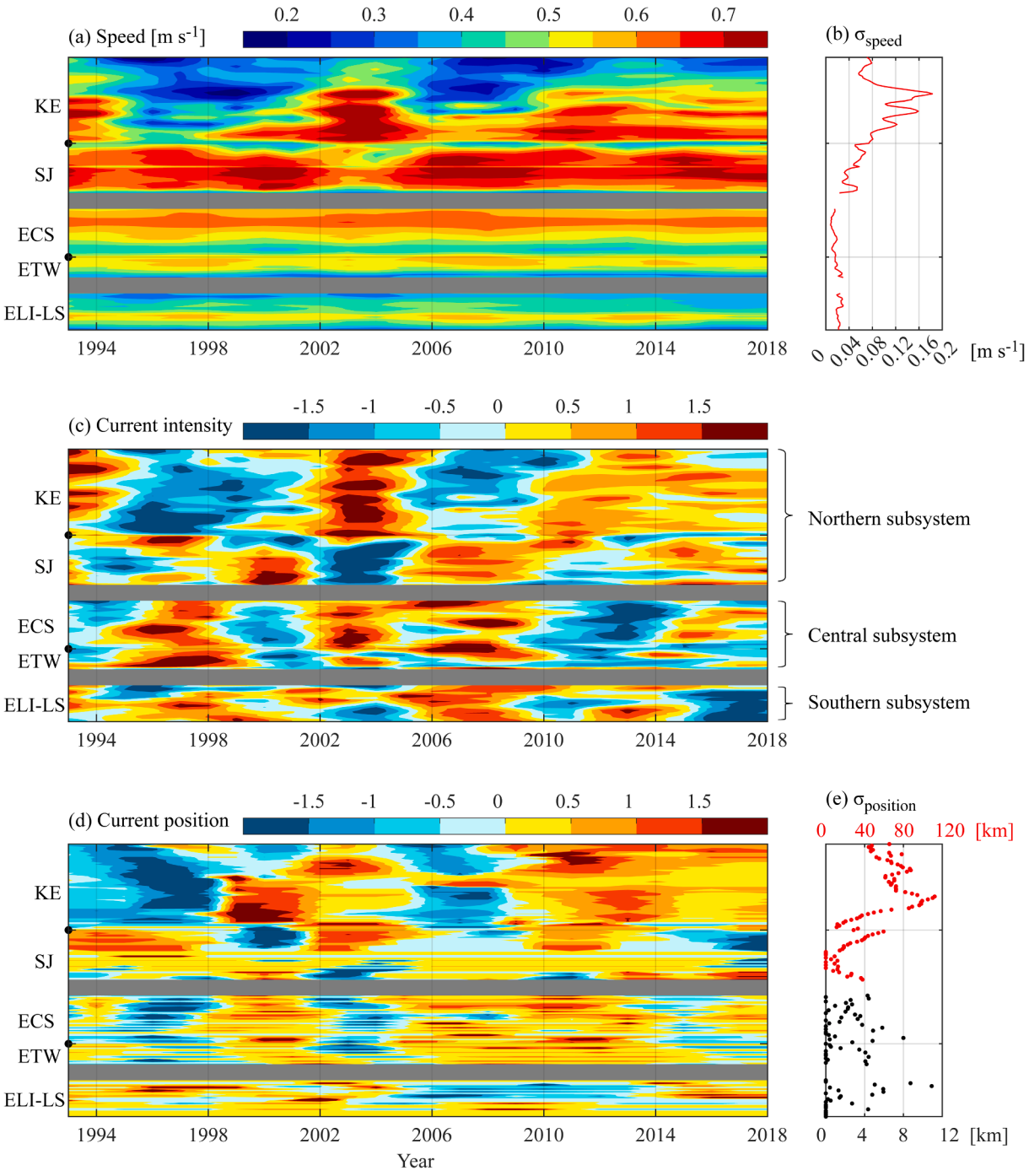

Fig. 5. (a) Hovmöller diagram showing temporal variabilities in the absolute sea surface geostrophic velocity (m s^{-1}) on the stream coordinate for the Kuroshio–KE System. (b) Standard deviations (m s^{-1}) of the geostrophic velocity in (a). (c) Hovmöller diagram showing the current-intensity variability on the stream coordinate for the Kuroshio–KE System; the current intensity was defined by normalizing the temporal variabilities in (a). (d) Same as in (c) but for the normalized current-position anomaly; positive (negative) values denote in-shoreward (off-shoreward) shift for the Kuroshio and northward (southward) shift for the KE. (e) Standard deviations (km) of the current-position variability in the distance; the lower and upper horizontal axes (unit: km) correspond to the black (ELI to ECS) and red dots (SJ to KE), respectively. (For interpretation of the references to color in this figure legend, the reader is referred to the web version of this article.)

3.2. Horizontal features of the synchronized variabilities and correlations with PDO_{SSH}

In this section, we exhibit horizontal features for the synchronized variabilities by using the composite analysis to first-mode principal components shown in Fig. 7. Hereafter, these first-mode principal components of the northern, central, and southern subsystems are expressed as PC-1_{NI}, PC-1_{CI}, and PC-1_{SI} for the current intensity, and as PC-1_{NP}, PC-1_{CP}, and PC-1_{SP} for the current position, respectively.

As shown in Fig. 6a, the SJ-Kuroshio intensity varied with an out-of-phase relationship with the KE intensity for the whole analysis period, whereas the comparison between Fig. 6a and b indicates that an out-of-phase relationship between the Kuroshio in the central subsystem and the KE existed in 2006–2014. More specifically, the comparison between Fig. 7a and b shows that a cycle PC-1_{NI} variability existing in 1996–2005 was incoherent with the PC-1_{CI} variability during the same period (see yellow-colored area), whereas the PC-1_{NI} during 2006–2014 had a coherent out-of-phase relationship with the PC-1_{CI} during the same

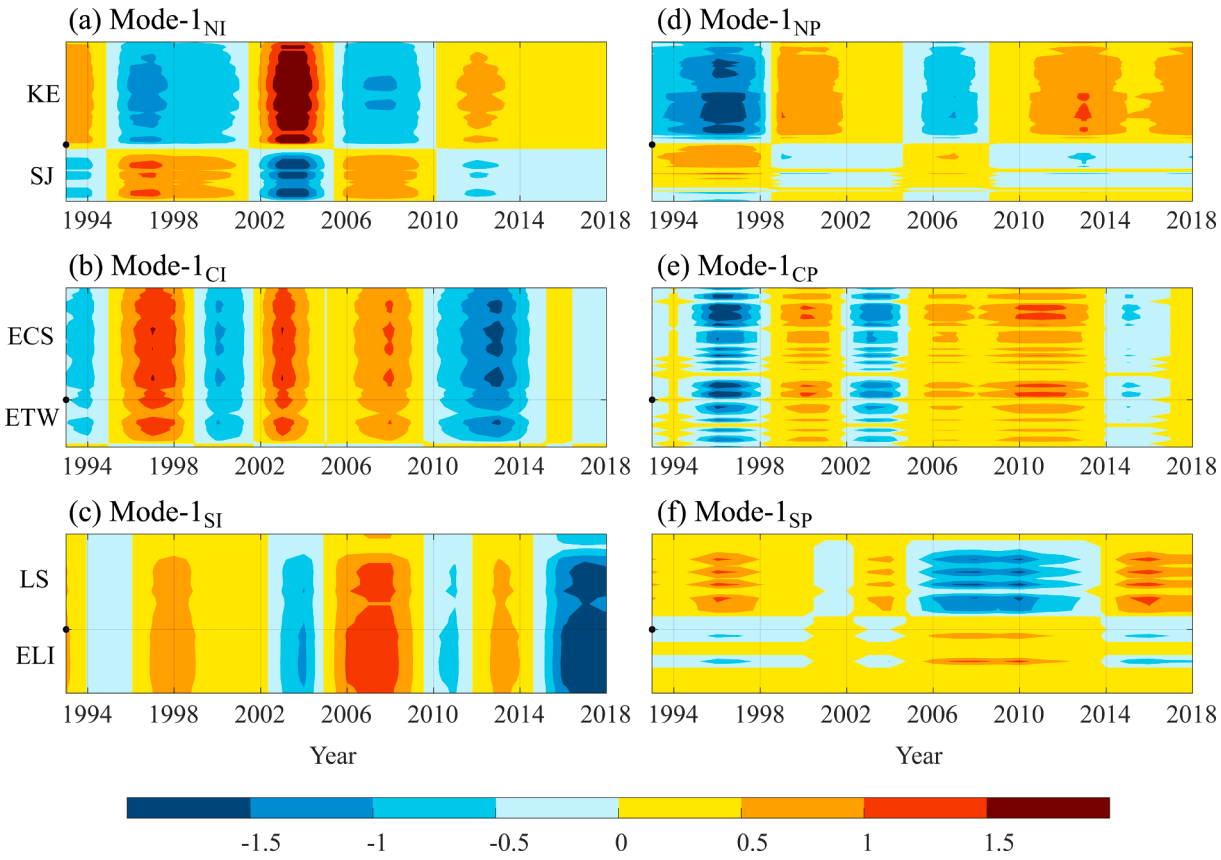

Fig. 6. (a)–(c) Reconstructions of current-intensity variabilities from EOF mode-1s for the (a) northern (mode-1_{NI}: 53.4%), (b) central (mode-1_{CI}: 55.6%), and (c) southern (mode-1_{SI}: 56.2%) subsystems. (d)–(f) Reconstructions of current-position variabilities from EOF mode-1s for the (d) northern (mode-1_{NP}: 44.0%), (e) central (mode-1_{CP}: 49.2%), and (f) southern (mode-1_{SP}: 40.2%) subsystems.

Table 1
Summary of the contribution ratios (%) of EOF mode-1, −2, and −3 to the total variance concerning each subsystem.

		Northern subsystem	Central subsystem	Southern subsystem
Current intensity	Mode-1	53.4	55.6	56.2
	Mode-2	15.6	16.5	15.4
	Mode-3	10.4	8.9	14.8
Current path	Mode-1	44.0	49.2	40.2
	Mode-2	20.9	11.3	19.2
	Mode-3	8.0	8.1	10.9

period (green-colored area). To clarify differences between the periods 1996–2005 and 2006–2014, we separately performed the composite analysis to the surface kinetic energy fields for the two periods. For the period 1996–2005, the surface kinetic energy difference between 2002 and 2005 (stronger KE) and 1996–2001 (weaker KE) is shown in Fig. 8a. As can be seen, the KE had an out-of-phase relationship with the SJ-Kuroshio. On the other hand, for the period 2006–2014, Fig. 8b showing the difference between 2011 and 2014 (stronger KE) and 2006–2009 (weaker KE) demonstrates that the KE had a clear out-of-phase relationship with the Kuroshio not only in the SJ but also in the central subsystem. Such an out-of-phase relationship between the KE and the Kuroshio in the central subsystem can be validated by a significant correlation coefficient between the PC-1_{NI} and PC-1_{CI} in 2006–2014 (−0.98, significant at 90% confidence level based on the Monte Carlo test).

The correlation coefficient between the PC-1_{CP} and PC-1_{SP} is −0.73 for the whole analysis period (i.e., 1993–2018) (significant at 90% confidence level based on the Monte Carlo test), implying that the Kuroshio shifted off-shoreward (in-shoreward) in the central subsystem while it shifted in-shoreward (off-shoreward) in the LS on a decadal timescale. Fig. 9 shows the SSHA difference and the velocity vector difference between the negative and positive PC-1_{CP} years around the Kuroshio in the central and southern subsystems (see the blue line in Fig. 7b); the Kuroshio in the central subsystem was strengthened along its offshore side but weakened along its inshore side, suggesting that the Kuroshio in the central subsystem shifted off-shoreward in the negative PC-1_{CP} years. Furthermore, Fig. 9 also shows that the Kuroshio took a path pattern that resembles a looping path (Fig. 3a in Nan et al. (2011)) in the LS during the negative PC-1_{CP} years. Therefore, we suggest that the Kuroshio paths were synchronized on a decadal timescale for the LS and the central subsystem, with a tendency that the looping path in the LS is associated with the off-shoreward shift of the Kuroshio in the central subsystem.

Table 2, summarizing correlation coefficients of the PC-1s with the PDO_{SSH} index (black lines in Fig. 7), clearly indicates that the PDO_{SSH} played a crucial role in the decadal variabilities of the Kuroshio–KE System. Regarding the synchronized variabilities:

(1) The relationship of the PC-1_{NI} to the PDO_{SSH} index was stationary for the entire period of 1993–2018, with the tendency that PC-1_{NI} lagged behind the PDO_{SSH} index by 3–4 years with a negative correlation, suggesting that the out-of-phase relationship

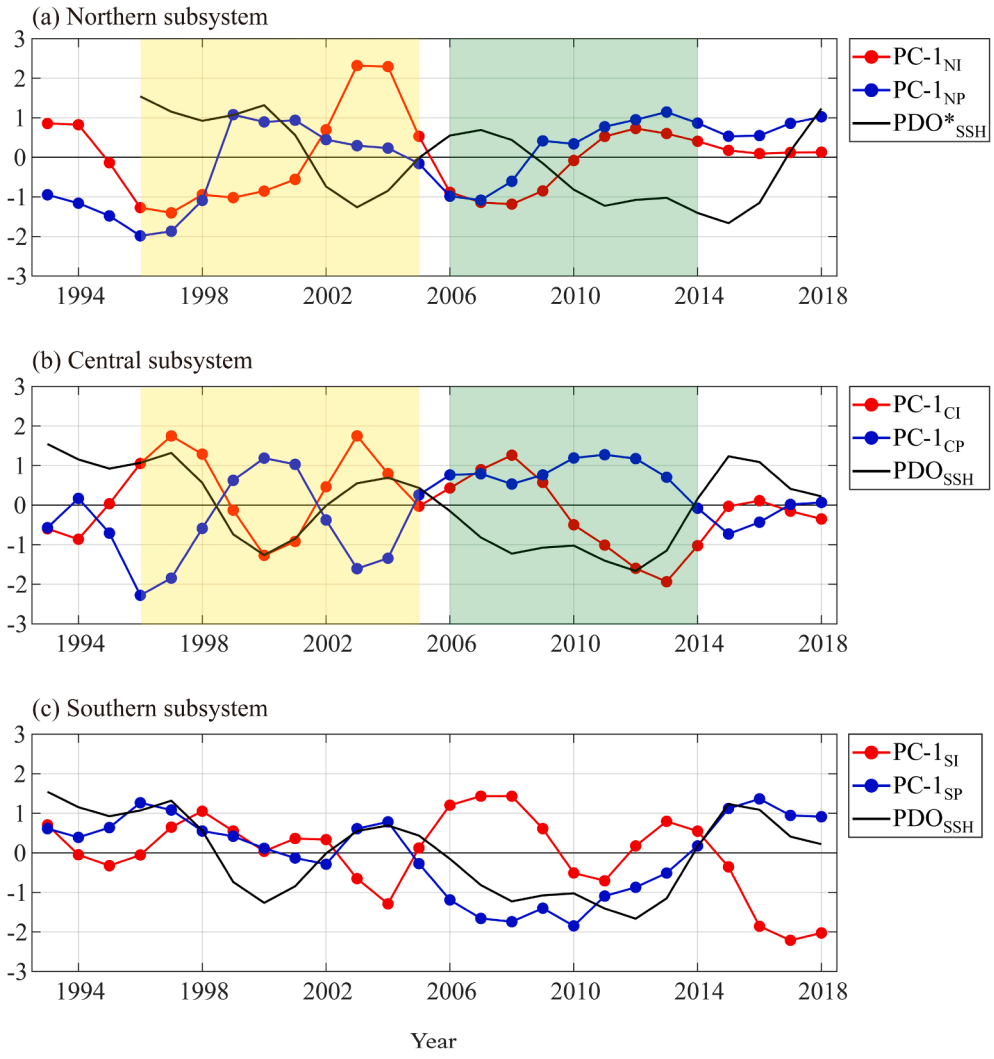

Fig. 7. Principal components of EOF mode-1s for the variabilities of current intensity (red lines) and current position (blue lines), along with the PDO_{SSH} index (black lines): (a) the northern subsystem, (b) the central subsystem, and (c) the southern subsystem. Note that the PDO^*_{SSH} in (a) denotes the PDO_{SSH} index moved ahead by 3 years. (For interpretation of the references to color in this figure legend, the reader is referred to the web version of this article.)

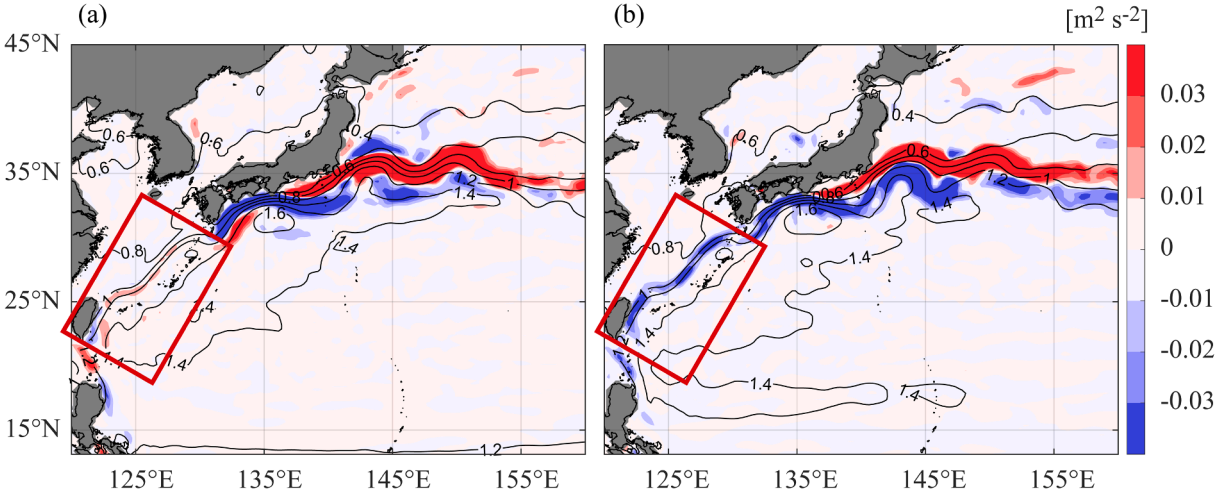

Fig. 8. (a) Horizontal distribution of the surface kinetic energy difference ($m^2\ s^{-2}$; color) between the periods 2002–2005 and 1996–2001 (the former minus the latter), along with the SSH (m; contour) averaged over both the periods. (b) Same as in (a), but for the periods 2011–2014 and 2006–2009.

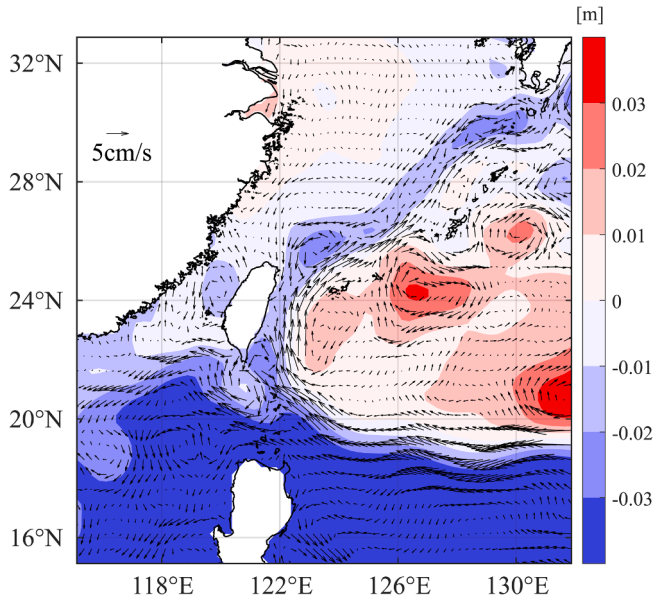

Fig. 9. Difference in the surface velocity fields (cm s^{-1}) between the negative and positive PC-1_{CP} years and the same difference of the SSHA (m) (the former minus the latter).

Table 2
Relationships of the current-intensity and current-position variabilities to the PDO_{SSH} index for each subsystem.

	Current intensity (CIN)	Current position (CPO)
Northern subsystem	CIN lags PDO_{SSH} by 3 or 4 years. (r = − 0.72 or − 0.70)	CPO lags PDO_{SSH} by 1 year. (r = − 0.57)
Central subsystem	In 1996–2005, positive no-lag correlation. (r = 0.89) In 2006–2014, CIN lags PDO_{SSH} by 3 or 4 years. (r = 0.89 or 0.97)	Negative no-lag correlation. (r = − 0.82)
Southern subsystem	Insignificant correlation. (r = − 0.28)	Positive no-lag correlation. (r = 0.78)

*Correlation coefficients (r) are indicated in parentheses, and they are all significant at 90% confidence level based on the Monte Carlo test except the CIN of the southern subsystem.

(Fig. 6a) between the KE and SJ-Kuroshio in the current intensity should be forced by the PDO_{SSH}.

(2) The relationship of the PC-1_{CI} to the PDO_{SSH} index changed from a positive simultaneous correlation in 1996–2005 to a positive 3–4 years lag correlation in 2006–2014. This transition resulted in the out-of-phase relationship between the KE intensity and Kuroshio intensity in the central subsystem during 2006–2014 (Fig. 8b).

(3) The PC-1_{CP} was negatively correlated with the PDO_{SSH} index, whereas the PC-1_{SP} was positively correlated with the PDO_{SSH} index, suggesting that the out-of-phase Kuroshio position relationship between the central subsystem and LS (Fig. 6e and 6f) should be forced by the PDO_{SSH}.

3.3. Decadal intensity variability in the northern subsystem

3.3.1. Mechanisms for the out-of-phase variability between the KE and SJ-Kuroshio

The dynamical processes were investigated for the out-of-phase relationship between the KE and SJ-Kuroshio in the current intensity. This relationship was characterized by a 3–4 years lag to the PDO_{SSH} index. To clarify this relationship, we regressed the SSHA upon the PC-1_{NI} (red line in Fig. 7a) with the PC-1_{NI} lagging the SSHA by 0–8 years (Fig. 10). Fig. 10a (0-yr lag) indicates that the area south of the KE (i.e., recirculation region south of the KE) was covered by positive SSHA (marked by a solid green closed curve), while the area south of the SJ-Kuroshio (i.e., recirculation region south of the SJ-Kuroshio) was covered by negative SSHA (marked by a dashed green closed curve). Such an SSHA distribution is responsible for the out-of-phase relationship between the KE and SJ-Kuroshio intensities. Fig. 10a–d implies the following process: the negative SSHA formed in the northeastern interior region (Area C in Fig. 4a) during the positive PDO_{SSH} phase (Fig. 10d) propagated westward for 3 years and weakened the KE (Fig. 10c); the negative SSHA then further migrated toward the recirculation south of the SJ-Kuroshio for 5 years and weakened the SJ-Kuroshio at 0-yr (Fig. 10a). Meanwhile, the positive SSHA formed in the northeastern interior region (Fig. 10b) during the negative PDO_{SSH} phase propagated westward for 3 years and strengthened the KE at 0-yr (Fig. 10a). The out-of-phase relationship between the KE and SJ-Kuroshio intensities could

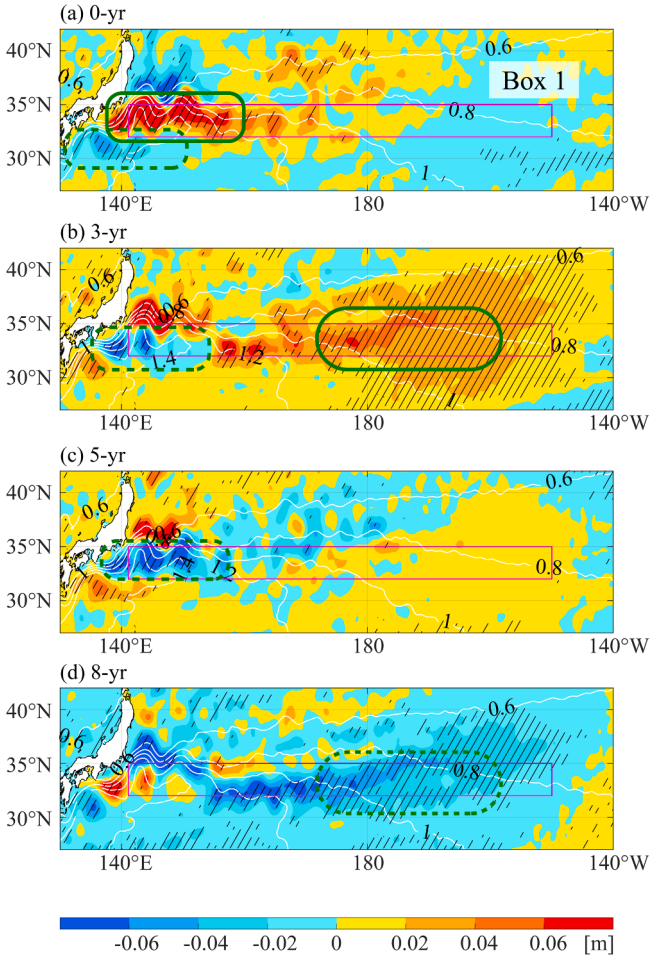

Fig. 10. Lag-regression coefficients (m) of the SSHA upon the PC-1_{NI}: (a) 0-yr lag (using 1993–2018 PC-1_{NI} and 1993–2018 SSHA), (b) 3-yr lag (1996–2018 PC-1_{NI} and 1993–2015 SSHA), (c) 5-yr lag (1998–2018 PC-1_{NI} and 1993–2013 SSHA), and (d) 8-yr lag (2001–2018 PC-1_{NI} and 1993–2010 SSHA). Distribution for the mean of the SSH is exhibited by white contours, and the areas with statistically significant correlation coefficients at the 90% confidence level based on the Monte Carlo test are shown by black hatchings. Positive (negative) SSHA focused on in the text is marked by a solid (dashed) green closed curve. The pink box (Box 1, 32°N–35°N, 141°E–150°W) denotes the domain for Fig. 11b and c. (For interpretation of the references to color in this figure legend, the reader is referred to the web version of this article.)

be formed because it took 5 years for both of the SSHA migration from the recirculation south of the KE to that south of the SJ-Kuroshio and the arrival of the next opposite-phase SSHA to the recirculation south of the KE (Fig. 10c to a); this concludes that the KE and SJ-Kuroshio intensity variabilities were simultaneously forced by two types of SSHA which were excited at the different PDO_{SSH} phases on a decadal timescale.

To confirm the driving mechanism of the PC-1_{NI} variability, we used the baroclinic Rossby wave propagation model described in Section 2.4. Fig. 11a shows the PC-1_{NI}, and Fig. 11b and 11c show longitude-time distributions for the SSHA modeled using Eq. (3) (c_R: 0.05 m s^{-1}) and those observed from satellite altimetry, respectively, both of which were processed with a 4 yr-low-pass filter and meridionally averaged within the Box 1 in Fig. 10a (i.e., 32°N–35°N, 141°E–150°W). Both the SSHA in Fig. 11b and 11c had a clear westward propagation with a tendency that positive (negative) SSHA correspond to positive (negative) PC-1_{NI}. With the consistency with the previous studies (Qiu, 2003; Qiu and Chen, 2005; Taguchi et al., 2007; Sasaki and Schneider, 2011; Sasaki et al., 2013; Sasaki et al., 2014), we can conclude that the PDO-related wind-forced baroclinic Rossby waves played the leading role in the decadal variability of the current intensity in the northern subsystem during 1993–2018. However, Fig. 11b indicates that modeled westward-propagating SSHA failed to reproduce a positive PC-1_{NI} in 2016–2018. Such an exceptional phenomenon is probably ascribed to the Kuroshio large meander event in the SJ since August 2017, as shown in Qiu et al. (2020).

An interesting phenomenon is that the SSHA had a slow southwestward migration along the south coast of Japan after the arrival of the baroclinic Rossby wave to the eastern coast of Japan (Fig. 10). The arrival of the next baroclinic Rossby wave with opposite SSHA formed the out-of-phase current-intensity relationship between the SJ-Kuroshio and the KE. This phenomenon is examined in more detail by performing the complex EOF (CEOF) analysis to the SSHA in the region of (125°E–160°E, 25°N–40°N) during 1993–2018; the CEOF analysis is a method to identify the propagating features in a temporal-spatial field. Fig. 12, showing the reconstructed leading CEOF mode accounting for 50.9% of the total variance, indicates that the SSHA continuously propagated southwestward from the recirculation south of the KE to that south of the SJ-Kuroshio with a decaying amplitude during the early migration stage but a growing one during the late stage. Although the dynamical mechanism of this slow southwestward SSHA migration is uncertain in the present study, we speculate that it might be caused by the combined effects consisting of the planetary Rossby waves and the nonlinear advection of two recirculations south of the KE and SJ-Kuroshio (see Fig. 8 in Jiang et al. (1995)). Furthermore, we consider that the coastal trapped wave propagating along the southern coast of Japan (Sasaki et al., 2014; Usui et al., 2020; Kida et al., 2020; Liu et al., 2021) is not a direct cause of the slow southwestward SSHA migration, because its wave speed is too fast to explain the nearly 5-year migration time. It is worth noting that both of the two SJ-Kuroshio large meander events (2004–2005 and after 2017) during the analysis period occurred after the arrivals of the negative SSHA to the recirculation south of the SJ-Kuroshio (signals C2 and C4 in Fig. 12); this, therefore, means that such negative SSHA arrivals were probably one of the factors triggering the SJ-Kuroshio large meander. In addition, Fig. 12 exhibits that the positive (negative) PC-1_{NI} phases corresponded to positive (negative) SSHA over the recirculation south of the KE and negative (positive) SSHA over the recirculation south of the SJ-Kuroshio. This consistency can be confirmed in Fig. 13: the temporal variability of the leading CEOF mode (Fig. 13a) was consistent in phase with the PC-1_{NI} (Fig. 13b), and the decreasing trend of the PC-1_{CEOF} amplitude (Fig. 13a) was consistent with the gradually weakened PC-1_{NI} amplitude (Fig. 13b).

To visualize temporal changes in activities of two recirculations south of the KE and SJ-Kuroshio, the strength anomaly index can be defined as.

$$S(t) = \iint_A \eta(x, y, t)\,dx\,dy, \tag{4}$$

where η denotes the SSHA, and A denotes the area where the SSH value

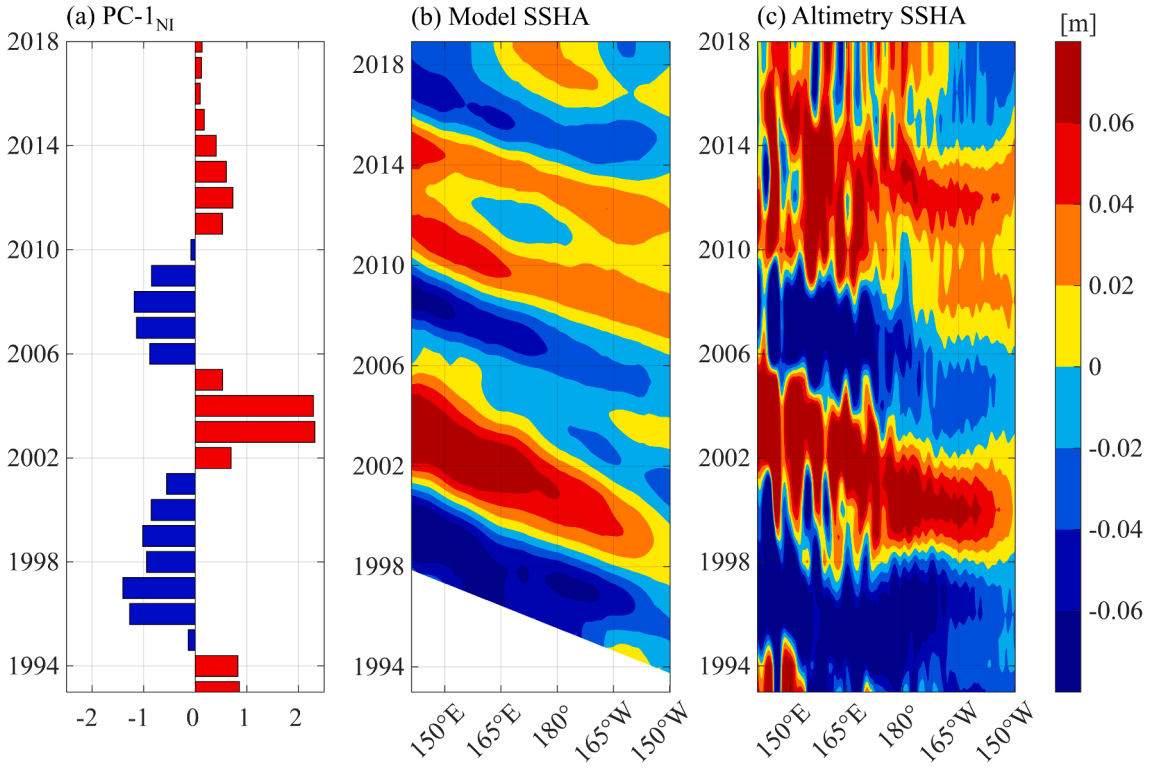

Fig. 11. (a) PC-1_{NI} is the same as the red line in Fig. 7a. (b)–(c) SSHA along the zonal band of (32°N–35°N, 141°E–150°W, Box 1 in Fig. 10a) from (b) Eq. (3) and (c) satellite altimetry data. (For interpretation of the references to color in this figure legend, the reader is referred to the web version of this article.)

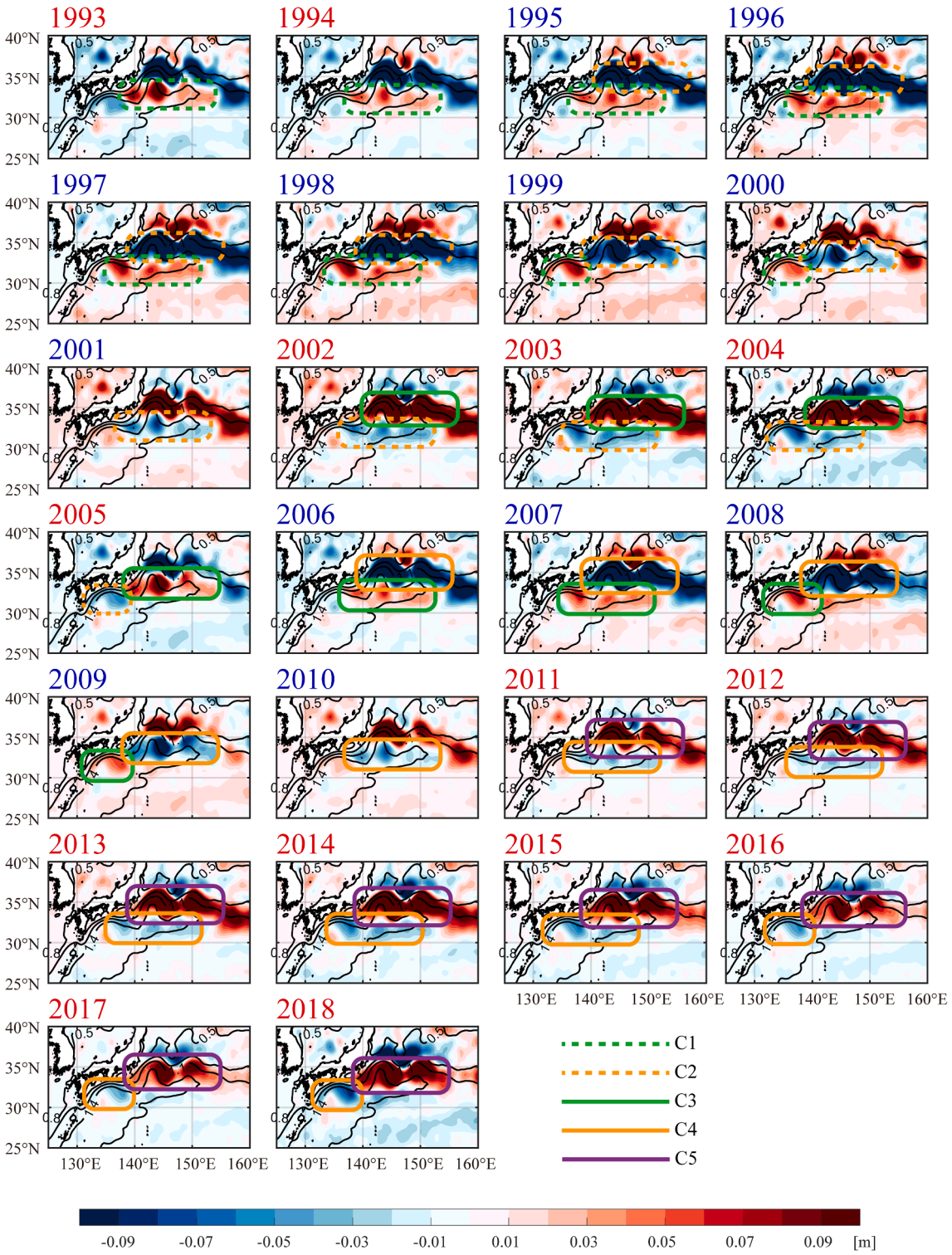

Fig. 12. SSHA distribution reconstructed from the leading CEOF mode (50.9%) of the SSHA in the region of (125°E–160°E, 25°N–40°N) during 1993–2018. SSHA migrations from the KE to SJ area are denoted by closed curves with names C1–C5, respectively. Red (blue) labels denote the positive (negative) PC-1_{NI} years. Black contours exhibit a mean SSH distribution during 1993–2018. (For interpretation of the references to color in this figure legend, the reader is referred to the web version of this article.)

exceeds 1.2 m inside of the KE region (blue rectangle in Fig. 2a: 32–38°N, 140–155°E) or SJ-Kuroshio region (red rectangle in Fig. 2a: 28.5–35°N, 131–139.5°E). As shown in Fig. 13, the positive (negative) PC-1_{NI} phase (Fig. 13b) almost corresponds to the positive (negative) phase of the KE recirculation strength (Fig. 13c) and the negative (positive) phase of the SJ-Kuroshio recirculation strength (Fig. 13d). This suggests that the SSHA affected the current intensity of the northern subsystem by strengthening or weakening the recirculation south of the SJ-Kuroshio and that south of the KE. Hence, the associated volume transport balance of the KE and SJ-Kuroshio can be maintained by including the two recirculations.

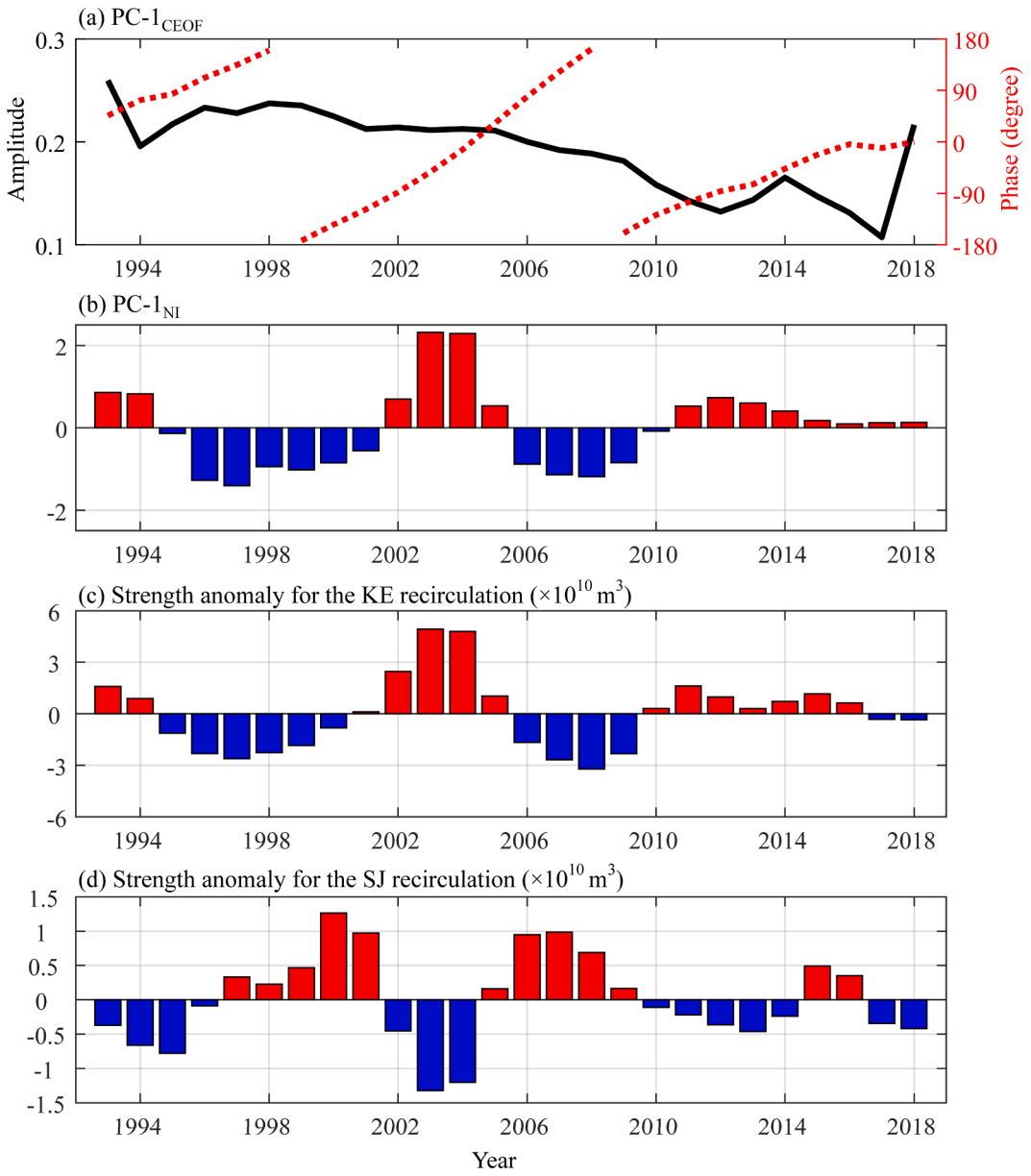

Fig. 13. (a) Temporal variability of the leading CEOF mode shown in Fig. 12 (PC-1_{CEOF}). Black (red) line denotes the amplitude (phase) of the PC-1_{CEOF}. (b) PC-1_{NI} (same as the red line in Fig. 7a). (c, d) Strength anomaly indices from Eq. (4) for the recirculations south of (c) the KE and (d) SJ-Kuroshio. The correlation coefficients are 0.96 between (b) and (c), −0.79 between (b) and (d), and − 0.66 between (c) and (d); all the correlation coefficients are significant at 90% confidence level based on Monte Carlo test. (For interpretation of the references to color in this figure legend, the reader is referred to the web version of this article.)

3.4. Decadal intensity variability in the central subsystem

Based on correlation coefficients of the PC-1_{CI} with the PDO_{SSH} index in different periods, we found that the relation of the decadal Kuroshio intensity in the central subsystem to the PDO_{SSH} index changed from a positive simultaneous correlation in 1996–2005 (r = 0.89, significant at 90% confidence level based on Monte Carlo test) to a positive 3 or 4 years lag-correlation in 2006–2014 (r = 0.89 or 0.97, significant at 90% confidence level based on Monte Carlo test). Such a transition implies that the decadal variability of the Kuroshio intensity in the central subsystem had undergone different effects between 1996 and 2005 and 2006–2014. Therefore, in this section, we investigate the mechanisms for these two periods separately.

3.4.1. Mechanisms for the variability in 1996–2005

To address this problem, we regressed the SSHA upon the PC-1_{CI} in 1996–2005, with the PC-1_{CI} lagging the SSHA by 0–3 years (Fig. 14). Fig. 14a indicates that the Kuroshio intensity variability in the central subsystem was related to the SSHA over both the STCC zone east of Taiwan and the inshore side of the Kuroshio in the ECS. Furthermore, Fig. 14a–d also implies that the Kuroshio intensity in the central subsystem was scarcely affected by the SSHA over the eastern North Pacific through a Rossby wave propagation.

It has been known that the number of anticyclonic eddies is larger than that of cyclonic eddies in the STCC zone east of Taiwan (e.g., Chow et al., 2017), so that the Kuroshio in the ETW and the upstream ECS is stronger during the eddy-rich period than the eddy-poor period (e.g., Yan et al., 2016, see their Fig. 11). We, therefore, thought that the decadal variability of mesoscale eddy activity in the STCC zone affected the decadal variability of the Kuroshio intensity in the central subsystem, and plotted the PDO_{SSH} index (Fig. 15a), the PC-1_{CI} denoting the Kuroshio intensity in the central subsystem (Fig. 15b), and the annual

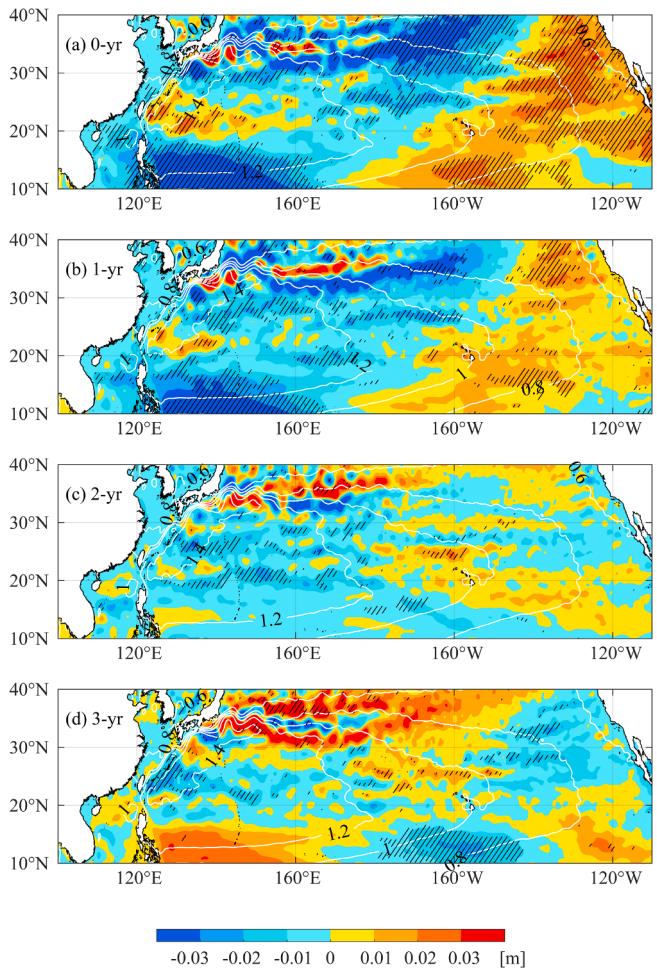

Fig. 14. Lag-regression coefficients (m) of the SSHA upon the PC-1_{CI} in 1996–2005: (a) 0-yr lag (using 1996–2005 PC-1_{CI} and 1996–2005 SSHA), (b) 1-yr lag (1996–2005 PC-1_{CI} and 1995–2004 SSHA), (c) 2-yr lag (1996–2005 PC-1_{CI} and 1994–2003 SSHA), and (d) 3-yr lag (1996–2005 PC-1_{CI} and 1993–2002 SSHA). Distribution for the mean of the SSH is exhibited by white contours, and the areas with statistically significant correlation coefficients at the 90% confidence level based on the Monte Carlo test are shown by black hatchings.

EKE anomaly (black line in Fig. 15c) averaged within the western STCC zone (21°N –25°N, 123°E–140°E). Here, the EKE was estimated using unfiltered monthly velocity data as follows:

$$EKE = \frac{1}{2}\left(u'^2 + v'^2\right), \tag{5}$$

where u' and v' are zonal and meridional velocity deviations from the mean, respectively. As shown in Table 3, all the correlation coefficients among these time series were positive and significant at the 90% confidence level based on the Monte Carlo test during 1996–2005. It can be, therefore, concluded that the eddy-rich (eddy-poor) situation around the STCC zone during the positive (negative) PDO_{SSH} phase strengthened (weakened) the Kuroshio intensity in the central subsystem for the period 1996–2005.

In addition, Fig. 14a implies that the PC-1_{CI} was negatively correlated with the SSHA in the western NEC zone (Area B in Fig. 4a), which is upstream to the Kuroshio, during 1996–2005. Therefore, it is reasonable to speculate that the negative SSHA inshore of the Kuroshio in the ECS was originated from the western NEC zone and moved to the ECS along the Kuroshio path. Although the connection between the ECS and western NEC zone is weakened near the ETW, this may be ascribed to mesoscale eddy activities east of the Luzon Strait and Taiwan. In Section 4.1, we will show the evidence that the SSHA migration along the Kuroshio path existed throughout the entire analysis period (i.e., 1993–2018) and discuss its migration speed.

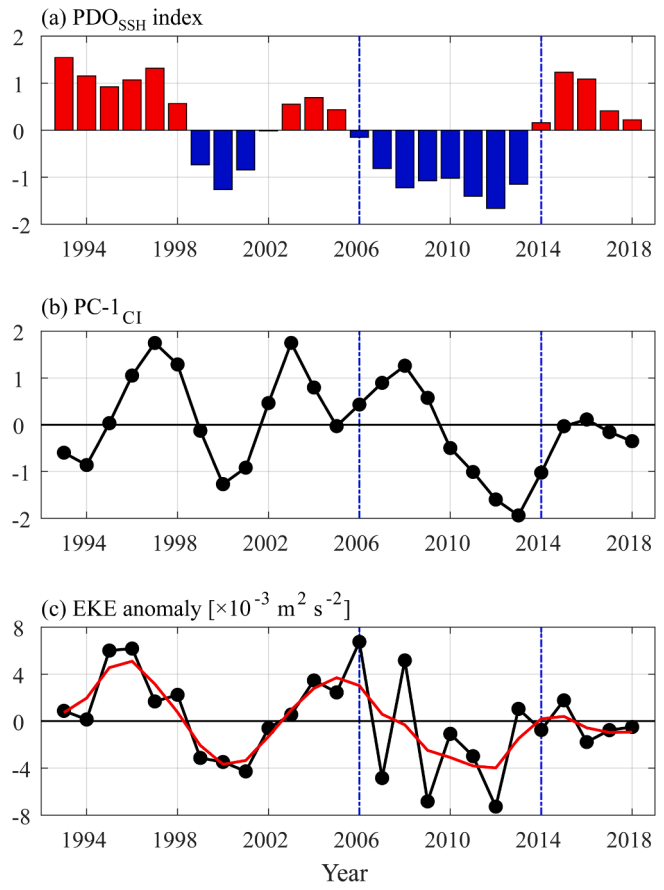

Fig. 15. (a) Annual PDO_{SSH} index. (b) PC-1_{CI} is the same as the red line in Fig. 7b. (c) The black line denotes the annual EKE anomaly averaged within the western STCC zone (21°N –25°N, 123°E–140°E); The red line denotes the result that the black line performed by a 4 yr-low-pass filter. (For interpretation of the references to color in this figure legend, the reader is referred to the web version of this article.)

Table 3
Correlation coefficients among the annual EKE (black line in Fig. 15c), PC-1_{CI} (Fig. 15b), and PDO_{SSH} index (Fig. 15a) for the periods 1996–2005 and 2006–2014. Confidence levels exceeding 90% are indicated in parentheses.

	1996–2005	2006–2014
Annual EKE & PC-1_{CI}	0.69 (>90%)	0.26
Annual EKE & PDO_{SSH}	0.89 (>90%)	0.43
PC-1_{CI} & PDO_{SSH}	0.89 (>90%)	0.19

3.4.2. *Mechanisms for the variability in 2006–2014*

During 2006–2014, all correlation coefficients among the PDO_{SSH} index, the annual EKE in the western STCC zone, and the PC-1_{CI} were statistically insignificant at a 90% confidence level based on the Monte Carlo test (Table 3). Note that the correlation coefficient between the PC-1_{CI} and decadal EKE variability (red line in Fig. 15c, which was obtained by applying the 4 yr-low-pass filter to the annual EKE time series) is 0.50 in 2006–2014 (insignificant at 90% confidence level based on the Monte Carlo test). Hence, Table 3 suggests that the mesoscale eddy activity in the STCC zone lost the effect on the decadal variability of the Kuroshio intensity in the central subsystem during this period.

The SSHA was regressed upon the PC-1_{CI} in 2006–2014, with the PC-1_{CI} lagging the SSHA by 0–3 years (Fig. 16). Fig. 16a indicates that the

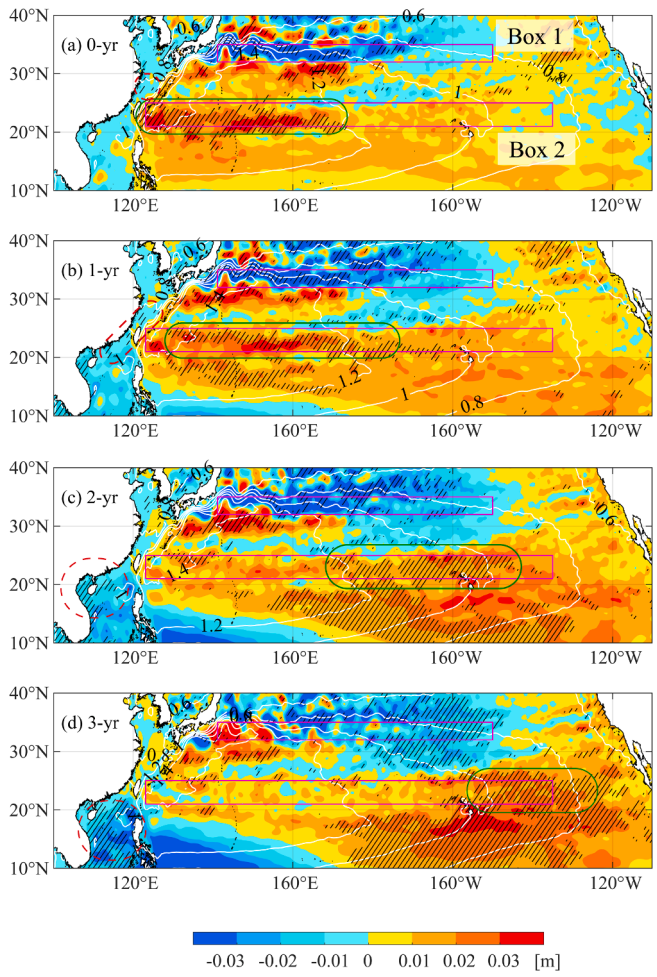

Fig. 16. Same with Fig. 14, but for the PC-1_{CI} in 2006–2014: (a) 0-yr lag (using 2006–2014 PC-1_{CI} and 2006–2014 SSHA), (b) 1-yr lag (2006–2014 PC-1_{CI} and 2005–2013 SSHA), (c) 2-yr lag (2006–2014 PC-1_{CI} and 2004–2012 SSHA), and (d) 3-yr lag (2006–2014 PC-1_{CI} and 2003–2011 SSHA). The Box 1 in Fig. 10 is also shown here, and the box over the low latitude (Box 2, 21°N –25°N, 123°E–135°W) denotes the domain for Fig. 17b and 17c. Positive (negative) SSHA focused on in the text is marked by a green (red) closed curve. (For interpretation of the references to color in this figure legend, the reader is referred to the web version of this article.)

PC-1_{CI} variability in this period was dominantly caused by positive SSHA extending from the STCC zone to the Kuroshio's offshore side in the central subsystem and secondarily affected by negative SSHA over the inshore side of the Kuroshio in the ECS. Fig. 16 implies a process that positive SSHA formed in the southeastern interior region (Area D in Fig. 4a) during the positive PDO_{SSH} phase (Fig. 16d) propagated westward through the STCC zone for 3 years and strengthened the Kuroshio in the ETW at lag 0-yr (Fig. 16a). Fig. 16a also indicates that the Kuroshio in the ECS was strengthened by the positive SSHA due to the Kuroshio's advection (see Section 4.1 for migration speed). Additionally, the slow southwestward SSHA migration along the southern coast of Japan might intrude partially into the ECS through the Tokara Strait at lag 1-yr (Fig. 16b). Furthermore, the negative SSHA formed in the South China Sea (SCS) (Fig. 16d) migrated to the ECS through the Taiwan Strait and strengthened the Kuroshio at lag 0-yr (Fig. 16a). This migration might be advected by the winter counter-wind current (e.g., Guan and Fang, 2006); this current can flow from the SCS to the ECS, passing through the Taiwan Strait, all year round. Meanwhile, the westward Rossby wave propagation of negative SSHA formed in the northeastern interior region (Area C in Fig. 4a) weakened the KE at lag 0-yr (Fig. 16).

The coherent westward propagations of two types of SSHA along the KE and STCC zones led to the out-of-phase relationship between the PC-1_{NI} and PC-1_{CI} during 2006–2014; the two types of SSHA were simultaneously excited in the eastern interior regions of the North Pacific during the same PDO_{SSH} phase (Fig. 4) and both of them needed ~ 3 years to reach the western boundary region (Fig. 16). Using Eq. (3) with c_R of 0.07 m s^{-1} at 23°N, we hindcasted the SSHA in the STCC zone (21°N –25°N, 123°E–135°W, the Box 2 in Fig. 16a) using monthly wind stress anomaly data. Fig. 17b shows the longitude-time diagram for the modeled SSHA (processed with a 4 yr-low-pass filter), and Fig. 17c shows the same SSHA derived from the satellite altimetry data. The PC-1_{CI} variability during 2006–2014 (Fig. 17a) could be well explained by the SSHA propagated from the southeastern interior region of the North Pacific for both the model (Fig. 17b) and observation (Fig. 17c). Specifically, wind-forced baroclinic Rossby waves with positive (negative) SSHA strengthened (weakened) the Kuroshio in the central subsystem during 2006–2009 (2010–2014). Finally, we point out that the mechanism governing the PC-1_{CI} in 2015–2018 had probably returned to that in 1996–2005: namely, the EKE activity in the western STCC zone (black lines in Fig. 17a) had been more effective on the decadal variability of the Kuroshio intensity in the central subsystem than the wind-forced Rossby wave propagation did (Fig. 17b).

4. Discussion

4.1. Mechanisms for the synchronized current-position variability between the central subsystem and LS

Current-position variabilities of the Kuroshio in the central subsystem and the LS were synchronized with an out-of-phase relationship (Fig. 6e and f), and this relationship was related to the PDO-related process. Because of the remarkably high correlation coefficients of the PDO_{SSH} index with the PC-1_{CP} ($r = -0.82$) and the PC-1_{SP} ($r = 0.78$), the PDO_{SSH} index can be used as a proxy for the current position of the Kuroshio. Fig. 18a, showing regression coefficients of the current cross-sectional speeds along the stream coordinate (Fig. 3) upon the PDO_{SSH} index, indicates that the Kuroshio shifted off-shoreward (in-shoreward) in the central subsystem but in-shoreward (off-shoreward) in the LS during the positive (negative) PDO_{SSH} phase. Additionally, the SSHA around the western boundary region was also regressed upon the PDO_{SSH} index (Fig. 18b). Negative SSHA covered the SCS during the positive PDO_{SSH} phase, which is likely directed the Kuroshio into the SCS in the LS based on geostrophy (Fig. 18a), resulting in the looping path structure of the Kuroshio in the LS on a decadal timescale (Fig. 9). Meanwhile, the Kuroshio region in the central subsystem was covered by negative SSHA during the positive PDO_{SSH} phase. This distribution strengthened the offshore side velocity of the Kuroshio while weakened its inshore side velocity, resulting in an off-shoreward shift of the current position in the central subsystem. The reverse was true for the negative PDO_{SSH} phase. Both Figs. 9 and 18b exhibit that a large fluctuation of the SSHA in the western NEC zone had a contribution to the downstream SSHA variability, suggesting that the Kuroshio position variability in the central subsystem was caused by the advection over the area from the western NEC zone to the ECS.

According to a two-layer planetary geostrophic model in Nakamura et al. (2007, see their Eq. (12)), the migration speed for such an SSHA along the Kuroshio path is approximately governed by three effects: barotropic current velocity, baroclinic topographic Rossby wave speed, and baroclinic planetary Rossby wave speed. It is, however, difficult to really estimate the propagation speed based on the model because the parameters used in the model are unknown. We, therefore, refer to an observed value as the SSHA migration speed along the Kuroshio path. Nakamura et al. (2003, see their Table 3) showed that the Kuroshio front meander with a horizontal scale of ~500 km has a phase speed of ~9 km day^{-1} near 28°N in the ECS. Using this value, the time in which the SSHA migrates from the ELI to the downstream ECS can be estimated as

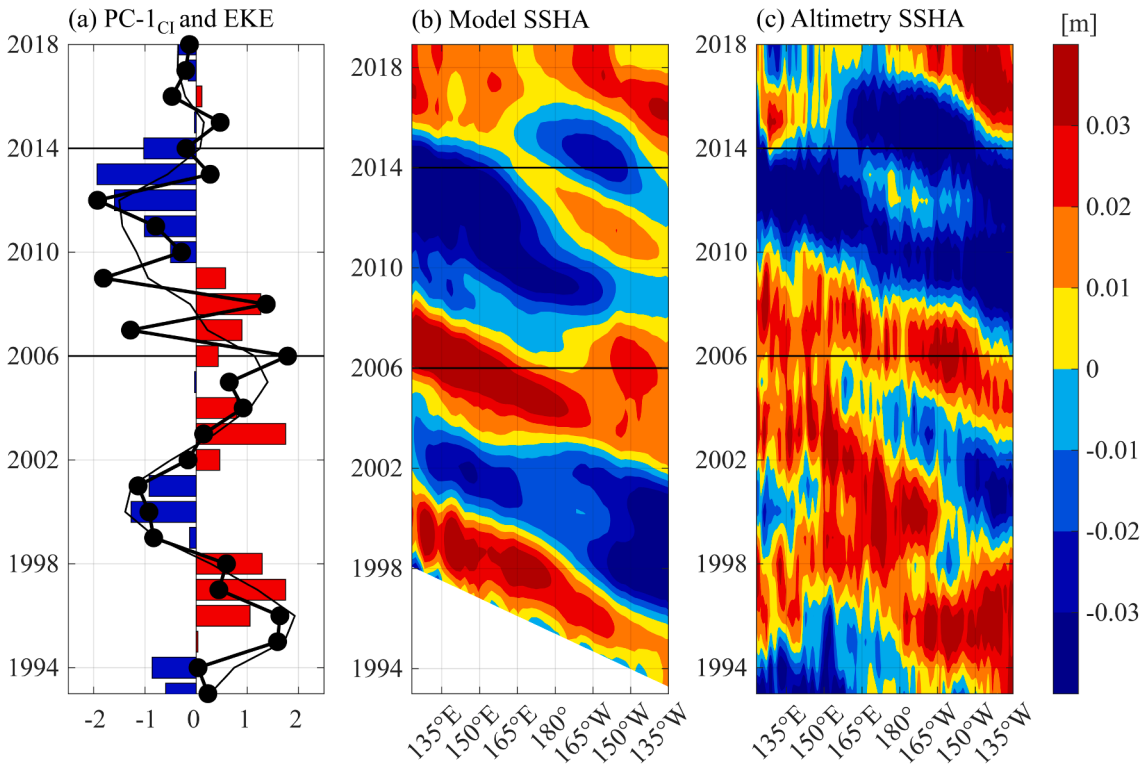

Fig. 17. (a) Bar denotes the PC-1_{CI} that is the same as the red line in Fig. 7b; the thick and thin lines show the normalized values for the black and red lines in Fig. 15c, respectively. (b)–(c) SSHA along the zonal band of (21°N –25°N, 123°E–135°W, Box 2 in Fig. 16a) from (b) Eq. (3) and (c) satellite altimetry data. (For interpretation of the references to color in this figure legend, the reader is referred to the web version of this article.)

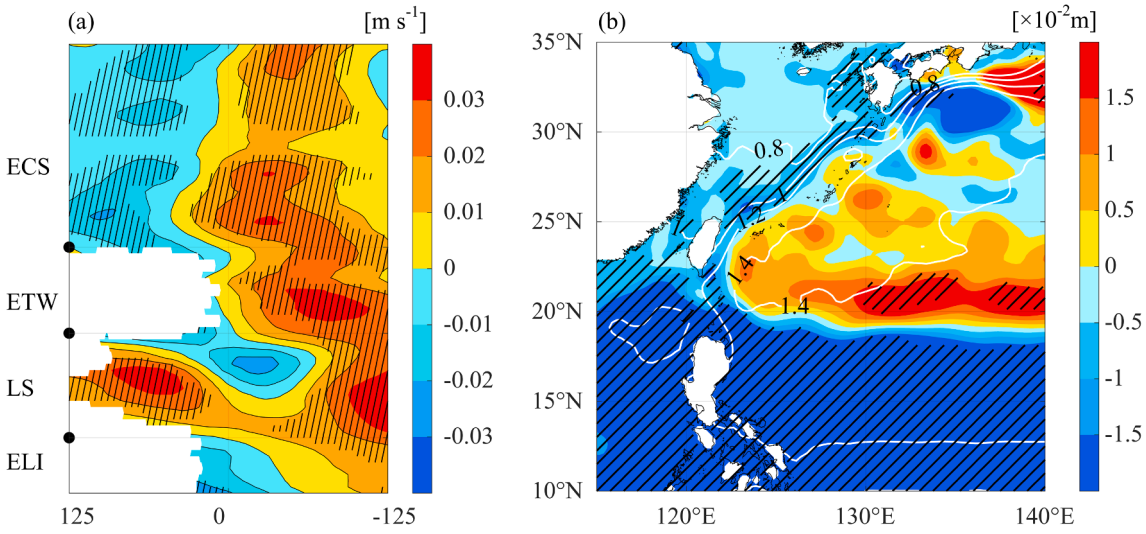

Fig. 18. (a) Regression coefficients (m s^{-1}) of the current cross-sectional speeds along the stream coordinate (Fig. 3) upon the PDO_{SSH} index. The x-axis represents the grid numbers on each cross-section; −125–0 (right side) denotes the offshore side, and 0–125 (left side) denotes the inshore side. (b) Regression coefficients (m) of the SSHA upon the PDO_{SSH} index in the western boundary region; the mean of the SSH is denoted by the white contours. Note that the areas with statistically significant correlation coefficients at the 90% confidence level based on the Monte Carlo test in both (a) and (b) are shown by black hatchings.

~200 days (i.e., ~1800 km distance/9 km day^{-1}). Therefore, it is reasonable to infer that the SSHA migrated from the western NEC zone to the ECS via the ETW within 1 year, even if the migration speed is assumed to be slower than ~9 km day^{-1} for disturbances with horizontal scales >500 km.

Based on the hypothesis of the gap-leaping effect on the Kuroshio induced by the upstream current speed (e.g., Sheremet, 2001), previous studies have suggested that the intrusions of the Kuroshio into the SCS through the LS, and intrusions onto the continental shelf northeast of Taiwan in the ECS, were related to a weakened current intensity of the Kuroshio (e.g., Wu, 2013; Wu et al., 2014, 2017; Liu et al., 2014; Yuan et al., 2014; Wang et al., 2016). For most of the analysis period, such a relationship could also be recognized in Fig. 7b and c. Here, it is worth noting that the relationship between the intensity and position of the Kuroshio in the central subsystem also had changed near 2006. As shown in Fig. 7b, the PC-1_{CI} and PC-1_{CP} had a clear out-of-phase relationship before 2006, but this relationship disappeared in 2006–2014. Instead, the PC-1_{CI} lagged the PDO_{SSH} index by 3 years, but the PC-1_{CP}

still maintained the negative no-lag correlation with the PDO_{SSH} in 2006–2014. Regarding this phenomenon, we speculate that the rapid SSHA migration from the western NEC zone to the ECS (Fig. 18b) changed the intensity (Section 3.4.1, Fig. 14a) and position of the Kuroshio simultaneously in the central subsystem during 1996–2005, whereas the arrival of the baroclinic Rossby wave during 2006–2014 changed only the Kuroshio intensity but not the current position, which was still determined by the SSHA migration from the western NEC zone to the ECS (Fig. 18b).

4.2. *Why the current-intensity variability during 2006–2014 was governed by baroclinic Rossby waves*

As indicated in Fig. 17 and Table 3, the current-intensity variability in the central subsystem was dominated by the decadal EKE variability in the western STCC zone during 1996–2005, whereas it was governed by the wind-forced baroclinic Rossby wave propagating along the STCC zone during 2006–2014. It is, therefore, still needed to be considered why the baroclinic Rossby waves became more important than the mesoscale eddies in 2006–2014.

The previous studies suggested that the prevailing wind patterns in both the tropical and subtropical North Pacific had changed since the 2000s. For example, Mochizuki and Watanabe (2019) exhibited that the trade winds strengthened since the 2000s; Wu et al. (2019) pointed out that the first EOF mode for the sea surface temperature anomaly over the North Pacific had been replaced by the second EOF mode since the 2000s, and this change in the leading mode was linked to the change in the sea surface wind field over the North Pacific; Liu et al. (2021) suggested that wind stress curl trend during the warming hiatus period (1998–2013) led to a Kuroshio weakening trend in the Tokara Strait of the ECS. It is, therefore, reasonable to infer that the prevailing wind pattern that had changed since the 2000s acted to intensify the baroclinic Rossby waves propagating along the STCC zone in 2006–2014. As shown in Fig. 17b, the wind-forced SSHA in the STCC zone was

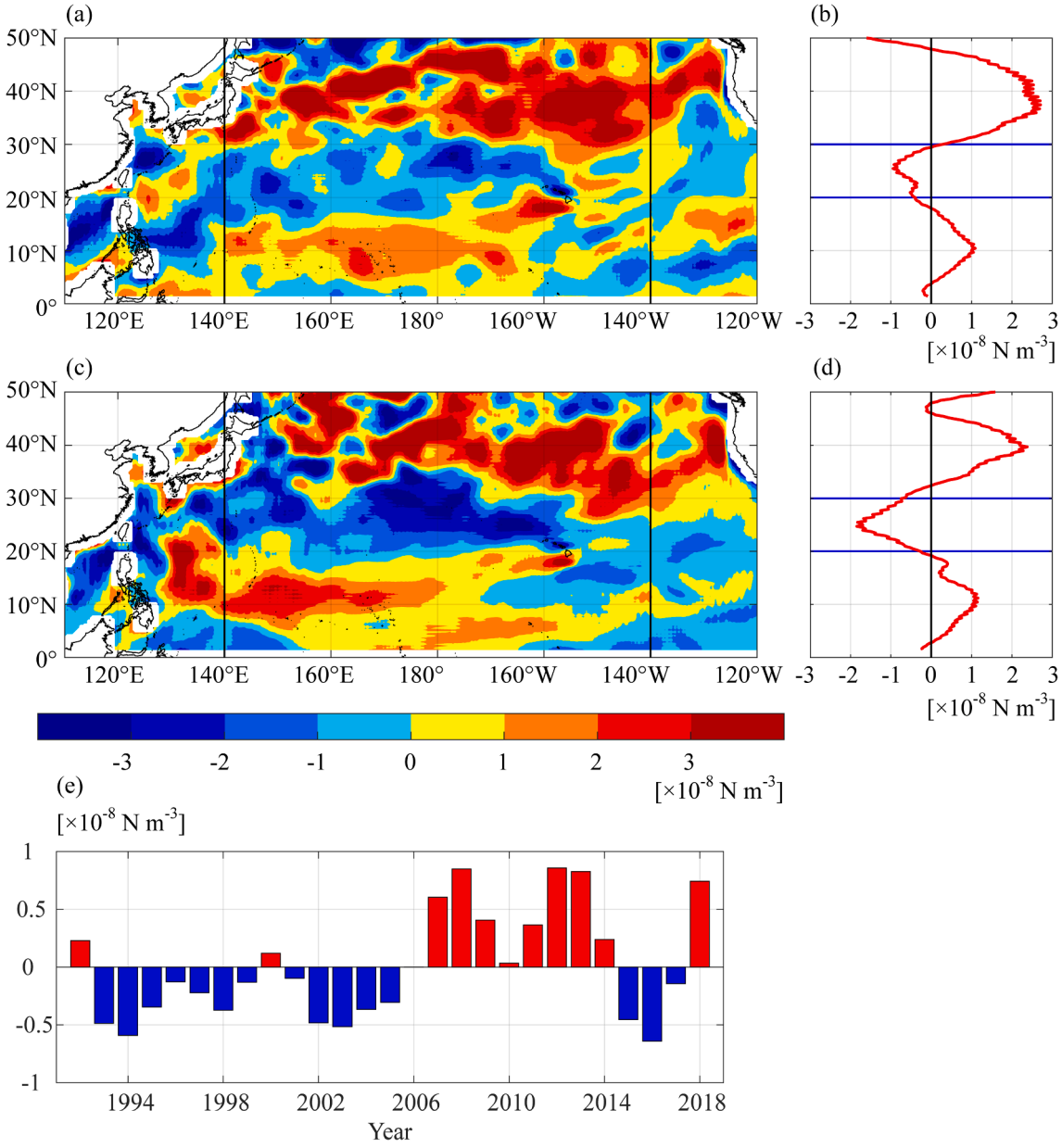

Fig. 19. (a) Difference of the wind stress curl anomalies in the North Pacific between the periods of 1993–1998 and 1999–2002 (the former minus the latter). (b) Zonally averaged values within 140°E–140°W for (a). (c) Same with (a) but for the periods of 2003–2005 and 2006–2013. (d) Same with (b) but for (c). (e) 4 yr-low-pass filtered wind stress curl anomaly averaged within Box 2 in Fig. 16a.

intensified from 2003; this intensification directly affected the decadal variability of the Kuroshio current intensity in the central subsystem from 2006 through the baroclinic Rossby wave propagation. Based on the phase of the PDO_{SSH} index, we calculated the difference of the wind stress curl between 1993 and 1998 and 1999–2002 over the North Pacific (Fig. 19a), and that difference between 2003 and 2005 and 2006–2013 (Fig. 19c). Fig. 19a and c indicate that the region of 20°N–30°N, which contains Box 2 in Fig. 16a, was occupied by the negative (positive) wind stress curl anomalies during the positive (negative) PDO_{SSH} period. It is worth noting that the negative wind stress curl anomalies within the area of (20°N–30°N, 140°E–140°W) in Fig. 19c are stronger than those anomalies in Fig. 19a. Furthermore, Fig. 19b and 19d indicate that the wind stress curl anomalies zonally averaged in 140°E–140°W were almost twice larger in 2003–2013 than in 1993–2002 over the area of 20°N–30°N. Fig. 19e, showing a 4 yr-low-pass filtered wind stress curl anomaly averaged within Box 2 in Fig. 16a, indicates that a long-lived negative wind stress curl anomaly over the STCC zone rapidly shifted to a positive anomaly around 2006; it is reasonable to infer that such a rapid phase shift with a relatively large amplitude triggered the effective baroclinic Rossby waves. Therefore, we insist that the rapid phase shift of the wind stress curl anomaly along the STCC zone around 2006 was the leading cause by which the baroclinic Rossby waves governed the Kuroshio current-intensity variability in the central subsystem during 2006–2014.

In addition, we point out that the EKE variability in the western STCC zone changed the timescale from the decadal to the interannual period since 2006 (Fig. 15c). Specifically, the annual EKE (black line in Fig. 15c) varied on a clear decadal timescale in 1996–2005, while it varied on an interannual time scale in 2006–2014 with a period of about 2–3 years. We, therefore, suggest that such a change in the STCC zone allowed the baroclinic Rossby waves to significantly affect the decadal current-intensity variability of the Kuroshio in the central subsystem. It is noteworthy that the high (low) frequency variability of the annual EKE in Fig. 15c was more dominant during the positive (negative) phase of the wind stress curl anomaly in the STCC zone (Fig. 19e). The dynamical linkage between the EKE timescale and wind field is beyond the scope of the present study, and thus it should be investigated in future studies.

5. Conclusions

In this study, using satellite altimetry and wind stress data, we presented the decadal variability of the Kuroshio–KE System in terms of its current intensity and position in a stream coordinate framework during 1993–2018, especially emphasizing the mechanisms generating the synchronized variabilities in the Kuroshio–KE System. Hovmöller diagrams (Fig. 5c and d), showing the temporal and spatial variability for the Kuroshio–KE System, indicated that Kuroshio–KE System comprised three subsystems characterized by coherent phase relations: namely, 1) northern subsystem where current intensities of the SJ and KE varied with an almost out-of-phase relationship, 2) central subsystem where current intensities of the ETW and ECS varied with a clear in-phase relationship, 3) southern subsystem where current intensities of the ELI and LS varied with an almost in-phase relationship. Based on the EOF analysis (Figs. 6 and 7) to each subsystem, we identified three types of synchronized decadal variabilities:

(1) The current intensity of the KE and SJ-Kuroshio varied with an out-of-phase relationship in the period 1993–2018. This coherency was forced by the westward-propagating baroclinic Rossby waves formed at the different PDO_{SSH} phases in the northeastern interior region. More specifically, after the arrival of the baroclinic Rossby wave to the recirculation south of the KE, the SSHA had a further southwestward migration toward the recirculation south of the SJ-Kuroshio within ~ 5 years, probably induced by the combined effects consisting of the planetary Rossby waves and the nonlinear advection due to two recirculations south of the KE and SJ-Kuroshio, as in Jiang et al. (1995). In the meantime, the next baroclinic Rossby wave carrying the opposite SSHA reached the recirculation south of the KE. Such an SSHA migration process caused the out-of-phase current-intensity relationship between the SJ-Kuroshio and KE.

(2) The current intensity of the KE and the Kuroshio in the central subsystem varied with an out-of-phase relationship during 2006–2014. This relation was mainly caused by the coherent westward propagations of two types of baroclinic Rossby wave along the KE and STCC zones, which were excited by the PDO-related wind forcing over the interior regions and STCC zone, and secondarily affected by the SSHA migration from the SCS to ECS through the Taiwan Strait (Fig. 16).

(3) The current path of the Kuroshio in the central subsystem and that in the LS varied with an out-of-phase relationship in the period 1993–2018. The former variability was caused by Kuroshio's advection, which rapidly carried the SSHA from the western NEC zone to the ECS within ~ 1 year, and the latter variability was affected by the SSHA localized in the SCS (Fig. 18).

Using data for the period 1993–2018, the present study also revealed that the correlation of the Kuroshio intensity in the central subsystem with the PDO_{SSH} index changed near 2006, unlike that in the northern subsystem was unchangeable in the same period (Table 2). The Kuroshio intensity in the central subsystem had a positive no-lag correlation with the PDO_{SSH} index in 1996–2005; such a correlation was caused by the decadal variability of the EKE in the western STCC zone, along with the influences of the SSHA migration from the western NEC zone (Fig. 14a and 15). However, it had a positive 3–4 years lag correlation with the PDO_{SSH} index during 2006–2014; this relation was caused by the amplification of baroclinic Rossby waves propagating along the STCC zone (Fig. 17); it was suggested that this amplification was generated by the rapid phase shift of the wind stress curl anomaly along the STCC zone around 2006 (Fig. 19). In addition, we pointed out that the mesoscale eddy activity in the western STCC zone lost the effect on the decadal variability of the Kuroshio intensity in the central subsystem during this period because the EKE variability in the western STCC zone had changed its timescale from the decadal to an interannual period near 2006 (Fig. 15c). Furthermore, we emphasized the effect of the SSHA advection from the western NEC on the decadal current-position variability in the central subsystem. A noteworthy point on this phenomenon is that the current-position variability in the central subsystem maintained the correlation with the PDO_{SSH} index even for the period 2006–2014, in which the current-intensity variability did not.

Last but not least, we summarize the problems that deserve future studies. Regarding the northern subsystem, the dynamical process of the SSHA migration from the recirculation south of the KE to the recirculation south of the SJ-Kuroshio still needs to be investigated (Figs. 10 and 12). Regarding the central subsystem, it is necessary to clarify the mechanisms for the incoherence between the decadal variabilities of current intensity and current position during 2006–2014 (Fig. 7b), and the reason why the timescale of the EKE variability in the western STCC zone had changed near 2006 (Fig. 15c). Regarding the southern subsystem, the formation and propagation mechanisms of the decadal SSHA variability in the SCS need to be more investigated in the future because such an anomaly is an essential driving force to the Kuroshio intensity in the ECS and the Kuroshio path in the LS. Finally, we address that the decadal variability of the Kuroshio intensity in the central subsystem probably changed its pattern near 2014, following the variability of the PDO_{SSH} index: namely, the Rossby-wave-regulated mode in 2006–2014 returned to the eddy-regulated mode as in 1996–2005. It is needed that we should carefully monitor this transition and consequent evolution to confirm whether the present mechanism is robust to the decadal variability of the Kuroshio–KE System.

Data Availability Statement

The datasets generated in the present study are available from the corresponding author upon request.

Declaration of Competing Interest

The authors declare that they have no known competing financial interests or personal relationships that could have appeared to influence the work reported in this paper.

Acknowledgments

We thank the handling editor and two anonymous reviewers for helpful suggestions and comments. This study benefited from fruitful discussions with Zhao-Jun Liu and Zhen-Long Zhang. This research was part of the dissertation submitted by the first author in partial fulfilment of a Ph.D. degree; all authors have provided consent.

Funding

This study was mainly supported by JSPS KAKENHI Grant Numbers JP22H04489, JP20H05169, JP19H05698, and the National Natural Science Foundation of China of China (41920104006).

References

Andres, M., Kwon, Y., Yang, J., 2011. Observations of the Kuroshio's barotropic and baroclinic responses to basin-wide wind forcing. J. Geophys. Res. 116 (C4) https://doi.org/10.1029/2010jc006863.

Chelton, D.B., Schlax, M.G., 1996. Global observations of oceanic Rossby waves. Science 272 (5259), 234–238. https://doi.org/10.1126/science.272.5259.234.

Chow, C.H., Tseng, Y., Hsu, H., Young, C., 2017. Interannual variability of the subtropical countercurrent eddies in the North Pacific associated with the Western-Pacific teleconnection pattern. Cont. Shelf Res. 143, 175–184. https://doi.org/10.1016/j.csr.2016.08.006.

Deser, C., Alexander, M.A., Timlin, M.S., 1999. Evidence for a wind-driven intensification of the Kuroshio current extension from the 1970s to the 1980s. J. Clim. 12 (6), 1697–1706. https://doi.org/10.1175/1520-0442(1999)0122.0.co;2.

Guan, B., Fang, G., 2006. Winter counter-wind currents off the southeastern China coast: A review. J. Oceanogr. 62 (1), 1–24. https://doi.org/10.1007/s10872-006-0028-8.

Han, G., Huang, W., 2008. Pacific decadal oscillation and sea level variability in the Bohai, yellow, and east China Seas. J. Phys. Oceanogr. 38 (12), 2772–2783. https://doi.org/10.1175/2008jpo3885.1.

Jiang, S., Jin, F., Ghil, M., 1995. Multiple equilibria, periodic, and aperiodic solutions in a wind-driven, double-gyre, shallow-water model. J. Phys. Oceanogr. 25 (5), 764–786. https://doi.org/10.1175/1520-0485(1995)0252.0.co;2.

Kida, S., Takayama, K., Sasaki, Y.N., Matsuura, H., Hirose, N., 2020. Increasing trend in Japan sea Throughflow transport. J. Oceanogr. 77 (1), 145–153. https://doi.org/10.1007/s10872-020-00563-5.

Liu, C., Wang, F., Chen, X., Von Storch, J., 2014. Interannual variability of the Kuroshio onshore intrusion along the East China Sea shelf break: Effect of the Kuroshio volume transport. J. Geophys. Res. Oceans 119 (9), 6190–6209. https://doi.org/10.1002/2013jc009653.

Liu, Z., Zhu, X., Nakamura, H., Nishina, A., Wang, M., Zheng, H., 2021. Comprehensive observational features for the Kuroshio transport decreasing trend during a recent global warming hiatus. Geophys. Res. Lett. 48 (18) https://doi.org/10.1029/2021gl094169.

Mantua, N.J., Hare, S.R., 2002. The Pacific Decadal Oscillation. J. Oceanogr. 58 (1), 35–44. https://doi.org/10.1023/a:1015820616384.

Mochizuki, T., Watanabe, M., 2019. Observed and hindcasted subdecadal variability of the tropical Pacific climate. ICES J. Mar. Sci. https://doi.org/10.1093/icesjms/fsz026.

Nakamura, H., 2020. Changing Kuroshio and its affected shelf sea: a physical view. In: Chen, C.T., Guo, X. (Eds.), Changing Asia–Pacific marginal seas. Springer, Singapore, pp. 265–305.

Nakamura, H., Ichikawa, H., Nishina, A., Lie, H., 2003. Kuroshio path meander between the continental slope and the Tokara strait in the East China Sea. J. Geophys. Res. 108 (C11) https://doi.org/10.1029/2002jc001450.

Nakamura, H., Ichikawa, H., Nishina, A., 2007. Numerical study of the dynamics of the Ryukyu current system. J. Geophys. Res. 112 (C4) https://doi.org/10.1029/2006jc003595.

Nakamura, H., Nishina, A., Tabata, K., Higashi, M., Habano, A., Yamashiro, T., 2012. Surface velocity time series derived from satellite altimetry data in a section across the Kuroshio Southwest of Kyushu. J. Oceanogr. 68 (2), 321–336. https://doi.org/10.1007/s10872-012-0101-4.

Nan, F., Xue, H., Chai, F., Shi, L., Shi, M., Guo, P., 2011. Identification of different types of Kuroshio intrusion into the South China Sea. Ocean Dyn. 61 (9), 1291–1304. https://doi.org/10.1007/s10236-011-0426-3.

Qiu, B., 2002. Large-scale variability in the Midlatitude subtropical and subpolar North Pacific Ocean: Observations and causes. J. Phys. Oceanogr. 32 (1), 353–375. https://doi.org/10.1175/1520-0485(2002)0322.0.co;2.

Qiu, B., 2003. Kuroshio extension variability and forcing of the Pacific decadal oscillations: Responses and potential feedback. J. Phys. Oceanogr. 33 (12), 2465–2482. https://doi.org/10.1175/2459.1.

Qiu, B., Chen, S., 2005. Variability of the Kuroshio extension jet, Recirculation gyre, and Mesoscale eddies on decadal time scales. J. Phys. Oceanogr. 35 (11), 2090–2103. https://doi.org/10.1175/jpo2807.1.

Qiu, B., Chen, S., 2013. Concurrent decadal Mesoscale eddy modulations in the western North Pacific subtropical gyre. J. Phys. Oceanogr. 43 (2), 344–358. https://doi.org/10.1175/jpo-d-12-0133.1.

Qiu, B., Chen, S., Schneider, N., Taguchi, B., 2014. A coupled decadal prediction of the dynamic state of the Kuroshio extension system. J. Clim. 27 (4), 1751–1764. https://doi.org/10.1175/jcli-d-13-00318.1.

Qiu, B., Chen, S., Schneider, N., Oka, E., Sugimoto, S., 2020. On the reset of the wind-forced decadal Kuroshio extension variability in late 2017. J. Clim. 33 (24), 10813–10828. https://doi.org/10.1175/jcli-d-20-0237.1.

Sasaki, Y.N., Minobe, S., Schneider, N., 2013. Decadal response of the Kuroshio extension jet to Rossby waves: Observation and thin-jet theory*. J. Phys. Oceanogr. 43 (2), 442–456. https://doi.org/10.1175/jpo-d-12-096.1.

Sasaki, Y.N., Minobe, S., Miura, Y., 2014. Decadal sea-level variability along the coast of Japan in response to ocean circulation changes. J. Geophys. Res. Oceans 119 (1), 266–275. https://doi.org/10.1002/2013jc009327.

Sasaki, Y.N., Schneider, N., 2011. Decadal shifts of the Kuroshio extension jet: Application of thin-jet theory*. J. Phys. Oceanogr. 41 (5), 979–993. https://doi.org/10.1175/2010jpo4550.1.

Sheremet, V.A., 2001. Hysteresis of a western boundary current leaping across a gap*. J. Phys. Oceanogr. 31 (5), 1247–1259. https://doi.org/10.1175/1520-0485(2001)0312.0.co;2.

Soeyanto, E., Guo, X., Ono, J., Miyazawa, Y., 2014. Interannual variations of Kuroshio transport in the East China Sea and its relation to the Pacific decadal oscillation and mesoscale eddies. J. Geophys. Res. Oceans 119 (6), 3595–3616. https://doi.org/10.1002/2013jc009529.

Sugimoto, S., Hanawa, K., 2011. Relationship between the path of the Kuroshio in the south of Japan and the path of the Kuroshio extension in the east. J. Oceanogr. 68 (1), 219–225. https://doi.org/10.1007/s10872-011-0089-1.

Taguchi, B., Xie, S., Schneider, N., Nonaka, M., Sasaki, H., Sasai, Y., 2007. Decadal variability of the Kuroshio extension: Observations and an eddy-resolving model Hindcast*. J. Clim. 20 (11), 2357–2377. https://doi.org/10.1175/jcli4142.1.

Usui, N., Ogawa, K., Sakamoto, K., Tsujino, H., Yamanaka, G., Kuragano, T., Kamachi, M., 2020. Unusually high sea level at the south coast of Japan in September 2011 induced by the Kuroshio. J. Oceanogr. 77 (3), 447–461. https://doi.org/10.1007/s10872-020-00575-1.

Usui, N., Tsujino, H., Nakano, H., Matsumoto, S., 2013. Long-term variability of the Kuroshio path south of Japan. J. Oceanogr. 69 (6), 647–670. https://doi.org/10.1007/s10872-013-0197-1.

Wang, Y., Wu, C., Chao, S., 2016. Warming and weakening trends of the Kuroshio during 1993–2013. Geophys. Res. Lett. 43 (17), 9200–9207. https://doi.org/10.1002/2016gl069432.

Wu, C., 2013. Interannual modulation of the Pacific decadal oscillation (PDO) on the low-latitude western North Pacific. Prog. Oceanogr. 110, 49–58. https://doi.org/10.1016/j.pocean.2012.12.001.

Wu, C., Hsin, Y., Chiang, T., Lin, Y., Tsui, I., 2014. Seasonal and interannual changes of the Kuroshio intrusion onto the East China Sea shelf. J. Geophys. Res. Oceans 119 (8), 5039–5051. https://doi.org/10.1002/2013jc009748.

Wu, C., Wang, Y., Lin, Y., Chao, S., 2017. Intrusion of the Kuroshio into the south and east China Seas. Sci. Rep. 7 (1) https://doi.org/10.1038/s41598-017-08206-4.

Wu, C., Wang, Y., Chao, S., 2019. Disassociation of the Kuroshio current with the Pacific decadal oscillation since 1999. Rem. Sens. 11 (3), 276. https://doi.org/10.3390/rs11030276.

Yan, X., Zhu, X., Pang, C., Zhang, L., 2016. Effects of mesoscale eddies on the volume transport and branch pattern of the Kuroshio east of Taiwan. J. Geophys. Res. Oceans 121 (10), 7683–7700. https://doi.org/10.1002/2016jc012038.

Yuan, Y., Tseng, Y.-H., Yang, C., Liao, G., Chow, C.H., Liu, Z., Zhu, X.-H., Chen, H., 2014. Variation in the Kuroshio intrusion: Modeling and interpretation of observations collected around the Luzon Strait from July 2009 to March 2011. J. Geophys. Res. Oceans 119 (6), 3447–3463.